THE UNIVERSITY *of* EDINBURGH

Edinburgh Research Explorer

Pressure and Thermal Characterisation of Dynamic Instabilities During Flow Boiling in Micro/Mini-channels at Different Azimuth Orientations

OPEN ACCESS

Pressure and Thermal Characterisation of Dynamic instabilities during Flow Boiling in Micro/Mini-Channels at Different Azimuth Orientations

Marius Vermaak[1], Daniel Orejon[2], Jaco Dirker[1], Khellil Sefiane[2], Josua P Meyer[1]

[1] University of Pretoria, Pretoria, South Africa

[2] Institute for Multiscale Thermofluids, University of Edinburgh, Edinburgh, United Kingdom

Abstract

Fluid instability was investigated experimentally during flow-boiling of Perfluorohexane (FC-72) in a flat horizontal micro/mini channel with a hydraulic diameter of 909 μm and an aspect ratio of 10 (5 mm x 0.5 mm). One-sided heating at different azimuth channel orientations (θ) in terms of gravity were considered, which ranged from bottom-heating ($\theta = 0°$) to top-heated ($\theta = 180°$) in 30° increments. Mass fluxes of 10, 20 and 40 kg/m²s were considered at a saturation temperature of 56 °C. Flow instability and the resulting thermal and pressure responses were identified and studied via high-speed video, infrared thermography, and pressure measurements. Various mass flux and heat flux combinations at each channel orientation leading to flow instabilities categorised into two-phase mixing, minor reverse flow and major reverse flow, were studied. Increased mass flux resulted in more frequent and more severe flow instability, irrespective of the channel orientation. Increased heat flux resulted in an increased number of operating conditions that were susceptible to flow instability, but the instabilities occurred at lower frequencies. In general, orientations that had a horizontal heated surface ($\theta = 0°$ and 180°) were most susceptible to flow instability, while the intermediate azimuthal rotations ($\theta = 30°$, 60° and 90°) exhibited flow instability only at the highest mass flux. It was also found that flow instability often resulted in improved heat transfer performance, particularly in regions of the channel that were occupied by liquid. Where-as no direct relationship between the mass flux and the heat transfer performance improvement could be identified, it was found that better heat transfer improvements were obtained at higher heat fluxes. At the highest mass flux, cases that were horizontal and heated from above ($\theta = 180°$) exhibited heat transfer coefficient improvements (during instability) of up to 77% and 275% in the single-phase and two-phase regions respectively compared to baseline stable conditions.

Keywords: *flow-boiling, instability, heat transfer, micro/mini channel, rotational orientation*

Nomenclature

a	Heat loss correlation coefficient
b	Heat loss correlation power
Bi	Biot number
c_p	Specific heat (J/kg·K)
f	Instability frequency (Hz)
g	Gravitational acceleration (m/s^2)
G	Mass flux (kg/m^{2}s)
h_{fg}	Latent heat of evaporation (J/kg)
H	Channel height (m)
I	Electric current (A)
k	Thermal conductivity (W/m·K)
l	Axial distance span per pixel (m)
L	Channel length (m)
$\dot{m}$	Mass flow rate (kg/m^{2}s)
n	Number of instability occurrences per experiment
P	Pressure (kPa)
$\dot{q}$	Effective heat flux (W/m^2)
$\dot{Q}$	Heat transfer rate (W)
t	Time (s)
T	Temperature (°C)
U	Voltage (V)
$\dot{V}$	Volumetric flow rate (m^3/s)
W	Channel width (m)
x	Width coordinate in channel (m)
y	Height coordinate in channel (m)
z	Axial coordinate in channel (m)

Greek symbols

α	Heat transfer coefficient (W/m^2·K)
$\Delta\alpha_\%$	Heat transfer coefficient improvement (%)
ρ	Density (kg/m^3)
θ	Azimuth rotational orientation angle (°)

Subscripts

b	Bulk fluid
h	Heated
in	Inlet
0	Outer / to the laboratory
out	Outlet
sat	Saturation
w	Inner wall

1. INTRODUCTION

Continuous miniaturisation of microelectronic components has resulted in a need for enhanced cooling solutions to improve electronic efficiency, to prevent localised overheating, and to reduce pre-mature component failure. For this purpose, active cooling methods utilise forced fluid motion to sustain increased convection heat transfer coefficients. Liquids are preferred to gasses as they have higher densities, heat capacities and thermal conductivities. Increasing a liquid's temperature to saturation conditions produce phase change which allow substantially more heat to be absorbed at a relatively constant surface temperature; this is known as flow boiling.

Liquids chosen for flow boiling applications are typically electrically inert, chemically stable and exhibits a boiling temperature between the atmospheric dew-point temperature and the recommended electric component peak temperature. These liquids are called refrigerants with a commonly used refrigerant being FC-72 which has a saturation temperature of approximately 56 °C at atmospheric pressure conditions [1]. Characteristics of flow boiling are affected by several factors including the inlet thermodynamic state, the heat flux, the operating pressure, the mass flux within the flow passage, the passage geometry (size and cross-sectional profile), and passage orientation. Density disparities between phases in flow boiling can result in secondary buoyancy-driven flow effects which are typically amplified at lower mass fluxes[2]. Therefore, bubble dynamics, as influenced both by the buoyancy and surface tension effects must be considered. Buoyancy effects can be amplified when the gravitational orientation of the system is carefully considered or is variable such as: on moving platforms like ships, planes, or laptops. Fixed orientation applications such as server rooms or data centres can leverage optimised orientations that amplify buoyancy effects.

Studies focusing on flow-passage orientation have traditionally considered the influence of the hydrostatic head by altering the height difference between the inlet and outlet. These changes in inclination refer to orientations from vertical up (+90°) to vertical down (-90°) which are compared against horizontal flow cases (0° inclination). Flow passages with large cross-sectional aspect ratios, and/or when non-uniform circumferential heating occurs, necessitate investigation in the azimuth rotational angle of the channel within the gravity field. Variable orientation systems will result in azimuth orientation changes which relate to scenarios such as heating from below (0°), from the side (90°), or heating from above (180°). Buoyancy effects on the heat transfer performance of a channel due to its inclination and azimuth orientation can be significant, depending on the channel size. Mini and macro channels typically see amplified buoyancy effects. Aspect ratio can significantly effect the heat transfer [3], aspect ratio changes occurring when high aspect ratio channels are rotated.

The flow state and geometric parameters mentioned earlier effect the time average heat transfer performance. Flow stability substantially influences the transient and the overall heat transfer. Because the wall heat transfer ability is so different between the liquid and vapour phase regions, knowledge of the phase distribution flow patterns, and level of confinement of vapour bubbles within the channel is vital. Compared to the length scales of typical bubbles in two-phase flow, the relatively small cross-sectional size of micro and mini-channels make them particularly susceptible to impacts of flow instability [4] which can result in different degrees (mild to severe) fluid motion fluctuations. Such fluctuations can cause mechanical vibrations which can damage components, produce noise in control sensors [5] and can result in variable heat transfer performance [6]. Under severe conditions the flow directions can temporarily reverse. Even in a single channel system, reverse flow and possible periodic dry-out on the heated wall can occur [7], which has a direct impact on the local governing flow regimes and the eventually burn-out or malfunction of the system.

3

Microchannel's susceptibility to flow instability necessitates constant monitoring of the instability to ensure the safe operation of the electronic cooling systems. One of the most common ways of monitoring flow instability is by analysing period and magnitude of pressure and temperature fluctuations, which are typically synchronised with one another allowing them both to be used as instability indicators [8]. In experimental investigations the prevalence, intensity and type flow instability are generally determined using pressure measurements. However, the implications of flow instability on the heat transfer (whether advantageous or detrimental) can only be determined by analysing the heat transfer surface temperature, and/or at the inlet and outlet fluid temperatures of the channel [9].Two generalised quantification methods exist with which to characterise the flow behaviour as either unstable or stable [8, 10, 11]: pressure-monitoring and visual inspection. Brutin, et al. [12] developed an analytical approach by considering fluctuations in the pressure difference over the channel. They used the average pressure difference value and a threshold value of ±1 kPa to indicate the occurrence of flow instability [13]. Celata, et al. [14] suggested that visual inspection be used to identify reverse and unstable flow behaviour, such as via the use of high-speed video [15]. Even though these methods are useful, there is a need to better understand the flow dynamics leading to instability events.

Visual interpretation of changes in flow regimes due to vapour backflow/reverse flow can be grouped to create flow stability maps and dry-out maps [16]. These maps indicate unstable and stable regions by using either the mass flux and vapour quality as coordinates, or the phase-change number and sub-cooling number [17]. The phase-change number is defined as ratio of the total input energy to the total energy required for complete boiling, whereas the subcooled number is the ratio of enthalpy required to a saturated state and the latent heat. Boure, et al. [18] determined that there are two categories of instabilities: static and dynamic instabilities. Static instability refers to a change in the base line steady state flow pattern, such as a change in the slug's vapour attached from the heated wall to the unheated wall. Dynamic instability on the other hand, occurs transiently and is caused by the vapour-liquid interaction.

Static instabilities typically occur over a period of minutes and present differently in single and multi-channel systems. Multi-channel systems likely experience flow maldistribution, also known as a Ledinegg instability [19]. Ledinegg instabilities in multichannel heat sinks are accentuated by increasing the number of channels [20] but can be managed by altering the inlet plenum's geometry [21]. Static instabilities single-channel systems present as changes in bubble confinement. The vapour bubble detachment from one wall and either suspension between the wide walls or an attach to a different side wall can have a large influence on the heat transfer performance. This is typically most important in non-uniformly heated systems where the bubble detaching from the heated wall may substantially improve the steady-state heat transfer performance of the system [22]. Dynamic instabilities are associated with short-period oscillations and high-amplitude changes in fluid properties, both of which are fluid and system dependent. Such instabilities can occur in both single and multichannel arrangements and exhibit rapid change of the bubble motion. This often alters the flow patterns, changes the level of confinement, and affects the vapour location in the channel. To detect and identify the dynamic instabilities, high-speed imaging and sensory equipment are required to observe the presence of the resulting pressure oscillations, density wave oscillations and thermal oscillations [18, 23]. The frequency and intensity of the dynamic instability are influenced by several factors. The instability frequency increases with reduced operating pressure and the mass flux [24], or increased heat flux [8]. The latter is dominated by nucleate boiling, particularly in cases of high

frequency. The instability intensity increases with the temperature difference between the wall and the fluid [25] which causes rapid vapour bubble expansion.

Flow instabilities are generally considered to be detrimental to the heat transfer performance of the channel due to the possible presence of localised dry-out conditions because of prematurely reaching the critical heat flux [26]. Ineffective heat transfer can thus be caused by elevated surface temperatures which can result in damage to, and burn-out of the system being cooled [20]. However, in some instances flow instabilities have been found to enhance the heat transfer performance of a flow boiling system. For instance: Maciejewska, et al. [27] investigated flow boiling in two parallel minichannels at a mass flux of 163 kg/m^{2}s and found that flow instability improved heat transfer performance at the onset of nucleate boiling. Improvements in heat transfer have also been found in arrays with 60 parallel microchannels at mass fluxes between 11 kg/m^{2}s and 44 kg/m^{2}s [28]. The conflicting findings about the effect of instability flow boiling on the effectiveness of the heat transfer suggests that further investigation and analysis is required. Mingchen, et al. [29] experimentally showed that channel inclination and rotation of a heat sink operated with R134a at mass fluxes of 370–1250 kg/m^{2}s significantly affected the heat transfer coefficient. They found that by heating a set of 20 square horizontal parallel microchannels (0.5 mm x 0.5mm) from below rather than from above, the heat transfer coefficient was up to 14% higher at low heat fluxes and 10% higher at high heat fluxes. Li, et al. [30] reported similar trends in their study of a non-uniformly heated microchannel (width 5 mm; depth 0.5 mm) at mass fluxes of 200–500 kg/m^{2}s of deionised water, with heat fluxes between 4 kW/m^2 and 25 kW/m^2. The study considered horizontal flow with heating from above and below. Li et al. found that when the microchannels were heated from below, the heat transfer coefficient was up to 20% higher than when they were heated from above. Increases in mass flux resulted in a decrease in the effect orientation had on the heat transfer coefficient improvement. Despite the work of Li, et al. [30] there are no other studies that have investigated how the heat transfer is affected by intermediate channel orientations.

Experimental investigations of flow boiling in microchannels often focus on high heat flux applications that require similarly high mass fluxes (300-1500 kg/m^{2}s). In low heat flux application, high mass fluxes are undesirable and waste energy due to bigger pumps and large system pressure rating requirements. By reducing the mass fluxes to around 10 kg/m^{2}s to 40 kg/m^{2}s, low heat flux applications can be investigated where low flow resistance to pressure changes can result in significant instability effects on the heat transfer performance. The focus of this study was to determine whether flow instability during flow boiling at different channel orientations can be beneficial or detrimental to the internal heat transfer within a mini/micro-scale channel. The influence of channel orientation on the frequency and magnitude of flow instability was thus investigated at different mass and heat flux combinations. In addition, little is known about the heat transfer performance of FC-72 in a high-aspect ratio micro/mini channel heated from one side.

2. EXPERIMENTAL APPARATUS

The experimental facility, located at the University of Edinburgh, is represented in Figure 1. It was operated with FC-72 (C$_6$F$_{14}$) as the working fluid. Even though the set-up has been described in previous published work [31], a brief overview is presented here.
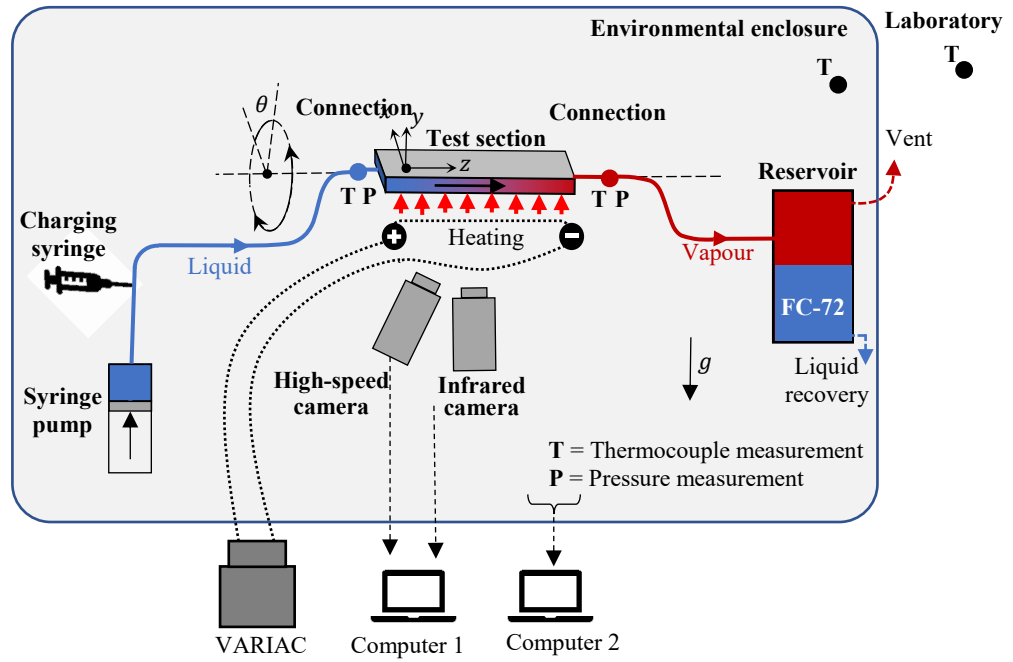
Figure 1: Schematic representation of the experimental setup

The main purposes of the set-up were to enable flow boiling, to visually observe the phase change process, and to employ infrared thermography at the heat transfer surface. The test sections orientation (inclination and azimuth rotation) could be adjusted depending on the test requirements. In this study, however, the channel was kept horizontal, i.e., no inclination, while the channel and imaging systems (oriented perpendicular to the heated wall) were rotated/adjusted around the flow axis to investigate different azimuth orientations (θ). The flow path consisted of a syringe pump, rigid and flexible tubing, an inlet connection assembly to the test section, the heated test section itself, the outlet connection test section assembly, more rigid and flexible tubing, and finally a collection reservoir. Inlet and outlet temperature and pressure measurement locations (indicated by "T" and "P" in Figure 1) were housed before and after the test section at the connection assemblies. High-speed video footage of the internal flow within the test section, as well as thermal infrared images of the heated side of the channel were recorded. The flow path and the cameras were accommodated inside an acrylic glass chamber to reduce thermal interference from the laboratory. A KDS 100 syringe pump (KD Scientific, USA) that had a screw-thread mechanism attached to a motor was used to move a plunger through a mounted glass syringe to push the FC-72 through the flow path. The syringe had an internal diameter of 34.2 mm (± 0.02 mm) and maximum volume of 100 ml. Volumetric flow rates with an accuracy of 1% between 0.1 μl/hour and 506 ml/hour could be achieved depending on the motor speed and size/internal diameter of the syringe. An additional hand-operated syringe was located close to the syringe pump outlet point to charge the set-up with fluid and to purge air from the system. The angle between bottom and top heated is defined as the azimuth angle. Bottom heated is an azimuth angle of 0° and top heated is an azimuth angle of 180°. A visual representation of a channel at an azimuth angle of 30° is shown in Figure 2 and the rotation of the test section in the experimental facility is also shown in Figure 3.
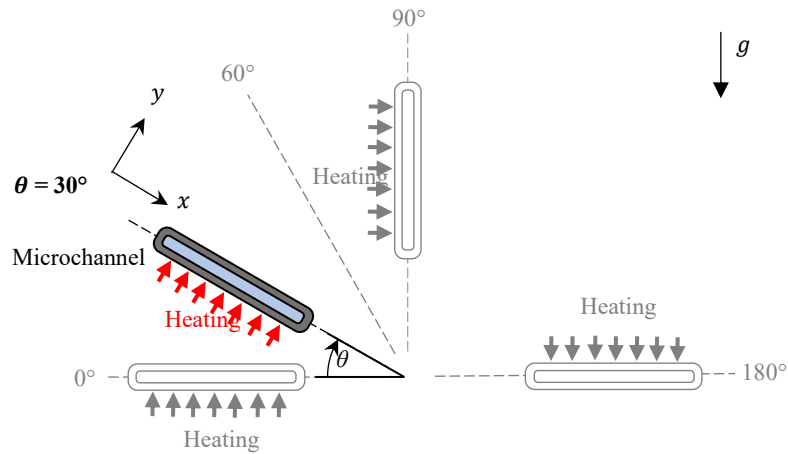
Figure 2: Channel azimuth angle indication

As mentioned, the inlet and outlet fluid temperature and pressure are measured in the connection outlet and inlet sections. See Figure 3 for the schematic's location for the pressure ports and thermocouples. For this purpose a T-type thermocouple of 0.2mm in diameter and an Omega® PXM219 gauge pressure transducer with a measuring range of 0 to 250 kPa with an accuracy of 0.025% of the full scale range [32] were used at each connection location. A detailed representation of the test section and the connection assemblies are shown in Figure 3. Liquid entered from the left and passed through a 10 mm sized T-type push-pull PEM0310W John Guest® fitting which acted as the inlet pressure port, as well as an L-type push-pull connection before entering the test section via a hollow borosilicate glass end-cap. Push-pull fittings lock inserted tubing in place and a release must be activated to remove the inserted tubing. These fittings minimize air leakage into the system or accidental disconnections occurring. The thermocouple leads, which had a diameter of 1 mm, pierced through the L-fitting (hole resealed with Araldite® Rapid epoxy) such that the measuring tip was fully located within the liquid at the centre of the end-cap. After the test section, the outlet connection had a similar lay-out.
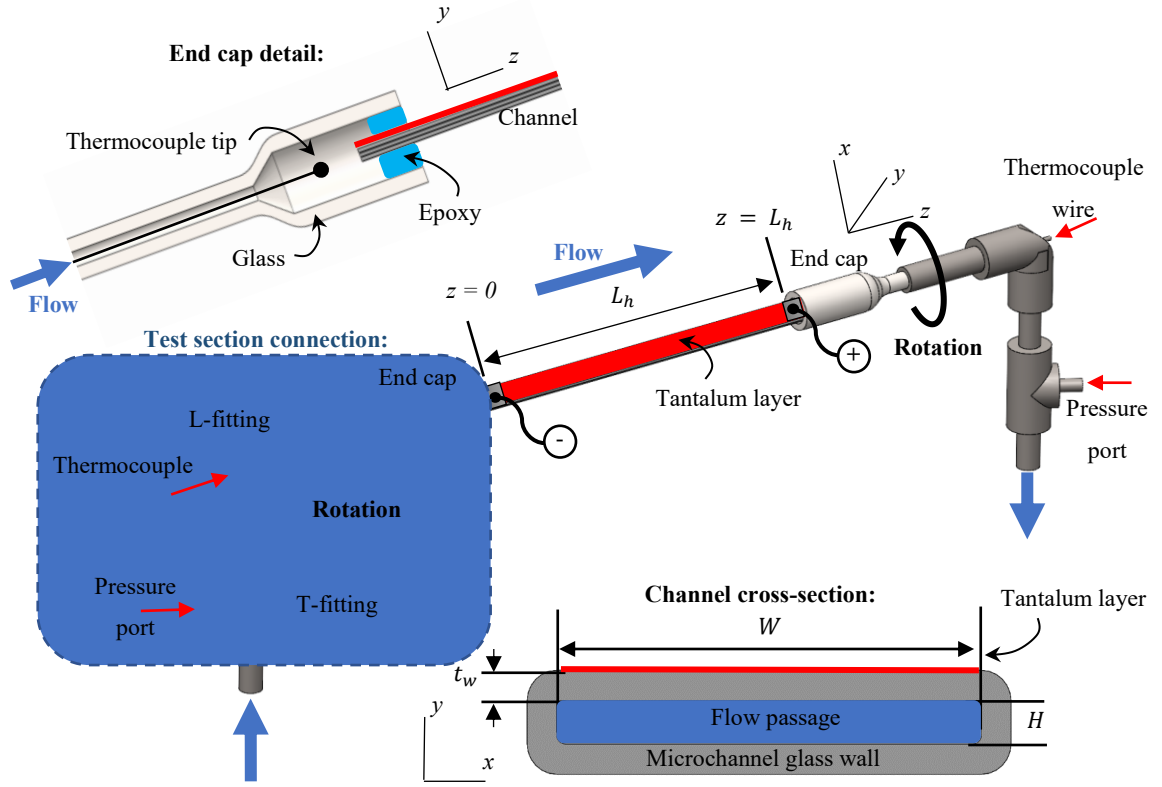
Figure 3: Tantalum-coated test section with its system connection assembly

The test section consisted of a rectangular glass channel. A set of channels was sourced from VirtoCom™, each with an axial length (L) of 100 mm ± 0.02 mm in the z direction, an inner width (W) of 5 mm ± 0.02 mm in the x direction, an inner channel height (H) of 0.5 mm ± 0.02 mm in the y direction, and a uniform wall thickness of t_w = 0.35 mm ± 0.02 mm. This resulted in a channel profile aspect ratio of 10 (width to depth) and a hydraulic diameter (d_h) of 909 µm. The dimensions were carefully selected to ensure that micro- and mini-scale physics dominated the bubble behaviour. The goal was to have a Confinement number greater than 0.5 so that confinement would be significant and the boiling would be dominated by nucleate boiling rather than convective boiling [33] ($Co = \frac{1}{d_h}\sqrt{\frac{\sigma}{g(\rho_l - \rho_v)}} = 0.797$), a hydraulic diameter of the same order of magnitude or less than the Laplace constant [34] ($L_{cap} = \sqrt{\frac{\sigma}{g(\rho_l - \rho_v)}} \approx 724 \ \mu m$) and a Bond number lower than 3 indicated mini channel physics will dominate [24] ($Bd = \frac{g(\rho_l - \rho_v)d_h^2}{\sigma} \approx 1.58$).

To enable single-sided Ohmic heating to study the effect of orientation and to permit optical visualisation from either side of the channel, a uniform thickness of 22.5 nm tantalum (Ta) metal was sputtered across the entire width and length of one side of the channel. At this thickness the tantalum is transparent allowing the visual observation of the fluid flow inside the channel. At this thickness the tantalum is transparent allowing the visual observation of the fluid flow inside the channel. Electric terminals consisting of aluminium foil were clamped onto the channel and connected to a variable current power source. The clamping distance influenced the heated length (L_h) which was between 75 to 80 mm long and resulted in an electric resistance of approximately 3.75 kΩ.

The endcaps, that each had a total length of 30 mm and an inner diameter of 6 mm at the channel connection point, were attached to the channel with Araldite® Rapid epoxy (melting temperature of 80 °C) to create an air-tight and liquid-tight seal. The inlet and outlet connection assemblies were attached via specially designed fastening blocks onto a side-mounted Axminster® rotary table.

The inclination of the test section could be adjusted via the rotary table, while the azimuth rotation orientation was adjusted by rotating the tube connections in the L-type fittings. The collection reservoir that received the vapour / liquid from the test section had a volume of 350 ml. Because it was vented to the outside of the laboratory, the fluid pressure inside the test section was at atmospheric pressure (approximately 101 kPa) and dictated a boiling temperature of approximately 56 °C, as is discussed in more detail later. Because the reservoir was at room temperature, the vapour from the test section condensed into liquid which was periodically drained from the reservoir and disposed responsibly. All components were connected via flexible tubing that had an internal diameter of 3 mm, external diameter of 5 mm and lengths of approximately 500 mm, before and after the test section from the syringe pump and to the collection reservoir respectively. The push pull fitting's internal diameter was greater than the external diameter of the flexible tubing requiring a section of rigid tubing to be the interfacial set up with an internal diameter of 5 mm external diameter of 10 mm and lengths of 5 cm.

A K-type thermocouple was placed on the rotary table to record the temperature in the enclosure while the laboratory temperatures were recorded with an additional K-type thermocouple on the outside of the acrylic glass enclosure. For flow visualisation, a high-speed Basler® acA800-510um CCD camera (Basler®, Germany) was used with a resolution of 800x600 pixels and maximum frame rate of 511 frames per second (fps). The lens used was a 12 mm fixed lens which had a wide enough viewing angle so that flow visualization of entire test section could be captured. The camera was placed perpendicular to the heated wall of the channel. The back side of the test section had a backlighting unit so that higher frame rates could be achieved. Infrared images of the heated wall were captured with a FLIR® A645 infrared camera (FLIR®, USA). The camera had a resolution of 640 x 480 pixels, a thermal sensitivity of 20 mK and maximum frame rate of 25 fps. Direct viewing of the test section resulted in self-generated reflections to be captured from the camera, creating inaccurate infrared images. The camera's lens had a viewing angle of 5° which was sufficient to prevent reflections from altering the temperatures of the infrared images.

A Clairtronic® 240V alternating current VARIAC transformer connected to a direct current (DC) rectifier was used to heat the test section. The rectifier was built by the electronics technical team at the University of Edinburgh. Current and voltage measurements were taken by MASTECH® MS8239 multimeters. The current was measured in mA and had an accuracy of 1%+0.1mA with a resolution of 0.01 mA. The voltage was measured in V with an accuracy of 0.5%+ 0.2V with a resolution of 0.1 V. Two data acquisition systems were used for the temperature and pressure data. Temperature data was recorded using a National Instrument® SCXI-100 chassis with a SCX1-1303 data card. Pressure measurements were recorded with a National Instrument USB-6008 stand-alone data acquisition unit. Both these units were connected to a computer running LabVIEW. High-speed images were recorded using the Basler's software Pylon Viewer. Infrared images were captured using ResearchIR software from FLIR®. High-speed images and infrared images were recorded on a separate system to that one recording temperature and pressure data.

3. EXPERIMENTAL METHOD

3.1 Calibrations

All the thermocouples were calibrated concurrently in an OPTIMA® T100 thermal water bath with a measurement uncertainty of ± 0.1 °C. Calibrations were done under steady-state isothermal conditions at temperatures between 20 °C and 60 °C in intervals of 5 °C. The reference temperature at each calibration point was the thermal bath's measured temperature. Steady state conditions at each set point was achieved by increasing the baths temperature to the desired temperature and then giving the deionised water 5 minutes to reach a uniform temperature in the bath and a steady temperature. Calibration measurements were taken at 100 Hz for 15 seconds at each temperature set point. This calibration process was completed prior to the first experiment and repeated after the final experiments had been conducted. No calibration drift was detected with the same calibration curve gradient and offsets identified. Calibration curves were used in LabVIEW to correct the raw recorded temperature data.The pressure transducers were calibrated *in situ*, positioned in the acrylic glass enclosure at the intended testing orientation using a SPER SCEINEFITIFC® Model 84083 manometer over the operating range of the study. Pressure transducer data was collected at 100 Hz for 15 s at each set point. Calibration correction functions were derived and directly imported into LabVIEW.

The Ta surface emissivity was determined using the technique described by Madding [33]. Temperature measurements from the tantalum surface were compared with the temperature on a surface with a known emissivity. Exact surface temperature were measured by K-type thermocouples placed on the two surfaces. The process was repeated at surface temperatures of 16°C and 35°C. The derived emissivity was found to be 0.8 (with an accuracy of 11%) which agreed with the emissivity of similar surfaces in previous studies [34-36]. Tertiary inputs to the infrared camera included temperatures of reflected surfaces, atmospheric temperatures, and the infrared camera's lens temperature. All these temperatures were assumed to be the same as the temperature inside the enclosure.

3.2 Test Matrix

The experimental test conditions for this study are presented in Table 1. All tests were conducted with FC-72 as the working fluid flowing in a horizontal channel at a saturation temperature (T_{sat}) of approximately 56 °C with an inlet fluid temperature (T_{inlet}) of approximately 19.5 °C. The latter was not controlled and was the same as the environmental temperature. Azimuth angles (θ) of 0°, 30°, 60°, 90° and 180°, and mass fluxes (G) of 10 kg/m²s, 20 kg/m²s and 40 kg/m²s were considered. Data was collected for θ = 120° and 150° but the results were inconclusive. Mass flux was defined as $G = \dot{m}/A_c$, with $A_c = WH$. The listed net heating fluxes at the wetted surface ($\dot{q}_{net}$) already includes the influence of heat loss to the testing enclosure (as is discussed in more detail later). These minimum heat flux depended on the operating mass flux and was based on the requirement for the onset of flow boiling within the test section. Subsequent heat fluxes (up to 7 different values) were determined at set intervals. Where applicable, heat fluxes were limited to ensure a Ta temperature of below 150 °C, which was the limit for the infrared thermography method.

Table 1: Test matrix

Parameter	Value range		
Fluid	FC-72		
Inclination orientation	Horizontal		
Saturation temperature (T_{sat})	56.25 °C ± 0.75 °C		
Inlet temperature (T_{in})	19.5 °C ± 3.5 °C		
Azimuth orientations (θ)	0°, 30°, 60°, 90° and 180° ± 1°		
Mass fluxes (G)	10 kg/m²·s	20 kg/m²·s	40 kg/m²·s
Associated net absorbed heat flux into fluid ($\dot{q}$)	3 – 7.3 kW/m²	5 – 13.8 kW/m²	9.6 – 15.1 kW/m²

3.3 Testing procedure

Before any tests were performed, possible contaminants were removed from the channel by first flushing the system with deionised water and then with air for 30 minutes. The channel was also dried by heating the facility to 36 °C for 5 minutes. To force out air, the flow path was temporarily charged with pre-boiled FC-72 while the channel was in a vertical orientation. Once the system was cleared of air, the channel inclination was adjusted back to be horizontal, and the desired azimuth angle orientation was set. The infrared and highspeed cameras orientation and positions were adjusted for each new orientation.

Because the test section was not thermally insulated from the testing cavity, convective heat loss from the hot Ta surface and the opposite channel surface were present. Since the net heat flux is needed to determine the heat transfer coefficient, heat loss rates had to be accounted for at each channel orientation. This was done by first conducting a series of steady state single-phase liquid experiments on the same test day prior to the main two-phase experiments. For this purpose, at each mass flux and test section orientation combinations in Table 1 five additional heat rates were considered. These heating rates were less than those associated with the cases in Table 1 in order to prevent flow boiling. From the single-phase data, a relationship between the surface temperature and the heat transfer rate into the air was established for temperature below the boiling temperature of FC-72 but extended to higher temperatures as described in more detail later.

The outlet thermocouple reaching a temperature of around 56 °C indicated that saturation conditions had been met in the test section and that further increases in heat flux would lead to a nucleation site forming somewhere on the heated surface. Small bubbles form at the nucleation sites, growing, and often detaching from the heated surface and moving in the direction of the flow. At insufficiently high heat fluxes, inconsistent vapour production from all nucleation sites led to all vapour exiting the channel. Further increases in the heat flux allowed for consistent vapour production from at least one nucleation site, this was defined as the incipience of boiling.

Once sufficient data was collected to describe the heat loss characteristics, the system was charged with analytically pure FC-72. The mass flow rate was adjusted to the desired value at the syringe pump and flow boiling was achieved by slowly increasing the heating rate. Data recording occurred once quasi-steady-state conditions were achieved, based on the outlet temperature when its value varied by less than 0.2 °C over a 3-minute period. Thereafter an additional 3-minutes period was allotted to ensure stable bubble dynamics within the test section before data was recorded during a 60-second experimental period, repeated twice for a total of 3 sets of data for each experimental condition. Instability events never lasted more than a few seconds allowing multiple instability events to be captured during a 60-second experimental period. The procedure was repeated for each mass flux.

4. HEAT TRANSFER COEFFICIENT ANALYSIS

Special care was taken to synchronise the time clocks on all the devices and computers used in this study. Because different logging frequencies were used for the recording of the pressure transducer and thermocouple data, and the infrared images, a MATLAB code was employed to align the starting time of each data set. The MATLAB code matched the timestamp of the first infrared image with the temperature and pressure data at the same stamp, allowing temperature, pressure and infrared data to be synchronised and used in the calculation discussed in the sections that follow. Infrared data was logged at a frequency that was at least four times slower than the thermocouple data and a linear change in the infrared temperature was assumed between the known intermediary time stamps.

4.1 Wall temperatures

In a typical infrared image, the heated surface of the test section coincided with 25 by 400 pixels (width by length). The outer Ta surface temperature, $T_h(x, z, t)$ varied in the x direction (across the channel width) and in the z direction (along the channel length), as well as with time (t). For any particular time-span, the local outer surface temperatures, $T_h(z)$, along the flow direction were calculated by taking the width-wise and time-step averages for each row of pixels. This resulted in approximately 400 wall temperature values along the heated length.

4.2 Heat flux

The local effective heat flux into the fluid, $\dot{q}(z)$, was determined by using the homogenous equilibrium model applied to axial distance spanned by one infrared image pixel (l):

$$\dot{q}(z) = \frac{\dot{Q}_h(z) - \dot{Q}_0(z)}{l \cdot W} \tag{1}$$

Here $\dot{Q}_h(z)$ and $\dot{Q}_0(z)$ are the locally applied heating rate and local heat loss rate to the environment per pixel span, and W is the width of the channel.

Because the applied electric heating resulted in a uniform flux along the full heated length, $\dot{Q}_h(z)$ for each pixel span was constant and was determined as follows:

$$\dot{Q}_h(z) = UI\left(\frac{L_z}{L_h}\right) \tag{2}$$

Here U and I are the voltage and current readings from the multi-meters, and L_h is the heated length.

The local heat loss per pixel span was calculated as follows:

$$\dot{Q}_0(z) = a[T_h(z) - T_0]^b \tag{3}$$

with $T_{h,z}$ the local average heated temperature across the width obtained from the infrared camera, and T_0 is the temperature inside the acrylic glass enclosure. $\dot{Q}_0$ is the amount of heat lost from the test section's heated length, a and b are both coefficients from the power function calculated from steady state experiments.

The data for the power function was obtained from the pre-test liquid-phase steady state conditions. The heat loss ($\dot{Q}_0$) for these cases were determined by applying the energy balance principle to the channel wall:

$$\dot{Q}_0 = U \cdot I - \dot{V}\rho c_P (T_{\text{out}} - T_{\text{in}}) \tag{4}$$

Here $\dot{V}$ is the pump volume flow rate, ρ is the fluid density, c_P is the fluid specific heat capacity, and T_{out} and T_{in} are the outlet and inlet fluid temperatures as obtained from the relevant test section connection thermocouples. Heat loss curves for all rotations tested are shown in Figure 4 at all heat fluxes tested. Mass fluxes are grouped together as the power loss between mass fluxes should be the same on the outer surface at the same temperature difference between the heated surface and the environment (ΔT).
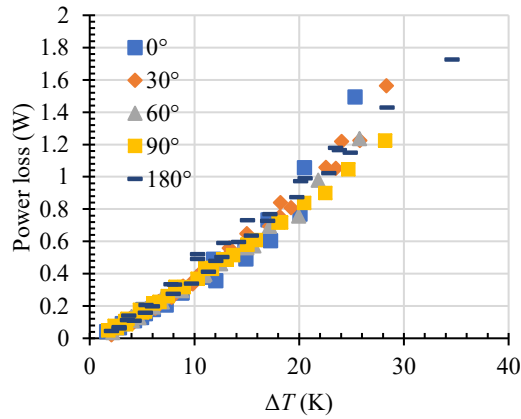

Figure 4: Power loss curves versus temperature difference for the channel at various orientations

The power loss to supplied power ratio varied greatly between rotation, mass flux and heat flux with around 10% to 50% of the power supplied is lost to the environment depending on the orientation tested. The maximum ΔT was 34 °C for the single-phase heat loss experiments and 125 °C for the two-phase experiments. The large number of ΔTs tested during the heat loss experiments allowed for a high-resolution heat loss curve to be produced for each orientation. Several studies show that a heat loss correlation for the lower portion of the temperature range would yield a similar result for the entire temperature range for linear, nonlinear, and exponentially fitted heat loss curves [37-40]. Thus, it was assumed that the power curves are applicable at higher temperature ranges as well.

The density and specific heat values were determined via correlations supplied by the fluid manufacturer 3M [1]. Those properties were evaluated initially at the inlet fluid temperature, at the local fluid temperature and the outlet thermocouple temperature once saturation conditions were reached:

$$\rho = 1740 - 2.61T \tag{5}$$

$$c_P = 1010 + 1.554T \tag{6}$$

Because the single-phase tests were conducted at 5 heat fluxes and at 3 mass flow rates, 15 data points were available for each channel orientation from which to obtain the values of a and b in equation (3) via regression analyses. The power curve form in that equation exhibited a good match with the convective and radiation heat transfer mechanisms and predicted the heat losses with an accuracy of 1.5% (or 0.1 W) for all wall temperature differences (between 5 to 50 °C) of the liquid-only cases.

4.3 Heat transfer coefficient

The local heat transfer coefficient along the axial coordinate $\alpha(z)$, was calculated from data of the heated side of the channel using equation (7). The average heat transfer coefficients are the arithmetic mean of the local heat transfer coefficients calculated in equation 7.

$$\alpha(z) = \frac{\dot{q}(z)}{T_{\mathrm{w}}(z) - T_{\mathrm{b}}(z)} \tag{7}$$

Here T_{w} is the inner wall temperature and T_{b} is the bulk fluid temperature. The local inner wall temperature was assumed to be the same as the measured local exterior wall temperature ($T_{\mathrm{w}} = T_{\mathrm{h}}$). This was checked by considering the local Biot numbers (Bi) for each pixel location (Equation 8). The Biot number provides the ratio between convective heat transfer and conductive heat transfer where 0.1 means that both heat transfer mechanisms contribute equally. The heated surface was modelled as semi-infinite plane wall where the characteristic length is half the wall thickness (τ_{wall}). The Biot number ranged from 0.03 to 0.3 in this study, with a $Bi \leq 0.1$ indicating that a maximum error of 5% would result from the uniform body assumption [41]. The time delay between the inner surface temperature changing and the outer measured surface temperature reaching that value was less than the period between infrared images for all Biot numbers, thus the uniform body temperature remained valid.

$$Bi = \frac{\alpha}{k} \cdot \frac{\tau_{wall}}{2} \tag{8}$$

The calculation of the local bulk fluid temperature was based on the thermodynamic properties of FC-72, the heat input per pixel span, and the mass flow rate. Due to the macroscopic nature of thermodynamic calculations, the obtained local bulk fluid temperatures along the channel length represented the average temperature of the fluid, and do not capture the fluid temperature variation within the cross-sectional profile of the channel. Because the FC-72 entered the test section as a subcooled liquid, there was a region where the fluid experienced sensible heating while it was still in its liquid phase and was characterised by an increase in the fluid temperature. However, once bulk (averaged) saturation conditions were reached, the average temperature remained constant at its saturation level (approximately 56 °C in this study).

The local bulk fluid temperature was expressed as follows, where $z = 0$ is at the start of the heated length.

For the liquid phase region ($T_{\mathrm{b}} < T_{\mathrm{sat}}$):

$$T_{\mathrm{b}}(z) = T_{\mathrm{in}} + \frac{W}{\dot{m}c_p} \int_0^z \dot{q}(z)dz \tag{9}$$

For the two-phase liquid-vapour (saturated) region:

$$T_{\mathrm{b}}(z) = T_{\mathrm{sat}} \tag{10}$$

where T_{sat} was determined by using the time-averaged outlet temperature measure of the thermocouple and cross-checked with the expected thermodynamic saturation temperature based on the atmospheric pressure. The measured outlet temperature was used as the saturation temperature in all calculations.

Because bubble dynamics and the local flow pattern in the channel affects the internal convection heat transfer coefficient, any instability event would result in variation in the heat transfer coefficient compared to conditions when the flow is stable. The percentage change in the heat transfer coefficient was calculated as follows:

$$\Delta\alpha_\% = \frac{(\alpha - \alpha_{\mathrm{ref}})}{\alpha_{\mathrm{ref}}} * 100 \tag{11}$$

where α_{ref} is the initial heat transfer coefficient the moment before the instability event occurred, while α is the maximum heat transfer coefficient within 1 second of the event. Instability events were defined based on an instability threshold. This threshold was defined using a combination of high-speed images and pressure transducer data. This is discussed in detail in section 5.4.

4.4 Uncertainty analysis

Measured inputs/outputs and calculated outputs had absolute and relative uncertainties which were calculated based on uncertainty measurement equipment by using the method developed by Moffat [42]. Results are presented in Table 2.

Table 2: Absolute uncertainties of the input parameters

Parameter	Relative error	Absolute error
Thermocouple temperature (T)		$\pm$ 0.14 °C
Uncalibrated infrared camera temperature (T_{h})		$\pm$ 2 °C
Heat absorbed (Q)		$\pm$ 0.16 W
Channel length (L)		$\pm$ 0.02 mm
Channel internal width (W)		$\pm$ 0.02 mm
Channel internal height (H)		$\pm$ 0.02 mm
Local distance from inlet (z)		$\pm$ 0.09 mm
Rotational orientation (θ)		$\pm$ 1°
Liquid density (ρ_{liquid})		$\pm$ 0.37 kg/m^3
Pressure (P)		$\pm$ 92 Pa
Voltage (U)	0.5%+0.2V (at resolution)	2.68 V

Current (I)	1%+1mA (at resolution)	1.75 mA
Heat flux ($\dot{q}$)	4.7%	0.13 kW/m^2
Volumetric flow rate ($\dot{V}$)	1%	2 ml/hr
Mass flux (G)	0.41%	0.16 kg/m^2·s
Heat transfer coefficient (α)	2%	6 W/m·K
Heat transfer coefficient improvement	3.1%	

5.   RESULTS

High-speed images, surface temperatures and pressure transducer measurements are presented in this section

5.1 Validation

This experimental procedure and the data processing technique was validated by making use of a uniformly heated case, and by comparing the thermal response with published results from literature. The average heat transfer coefficient (along the whole heated length) is shown in Figure 5 for an arbitrary case-set at various heat fluxes. It can be seen that good agreement was achieved both in terms of quantitative and qualitative measurements.
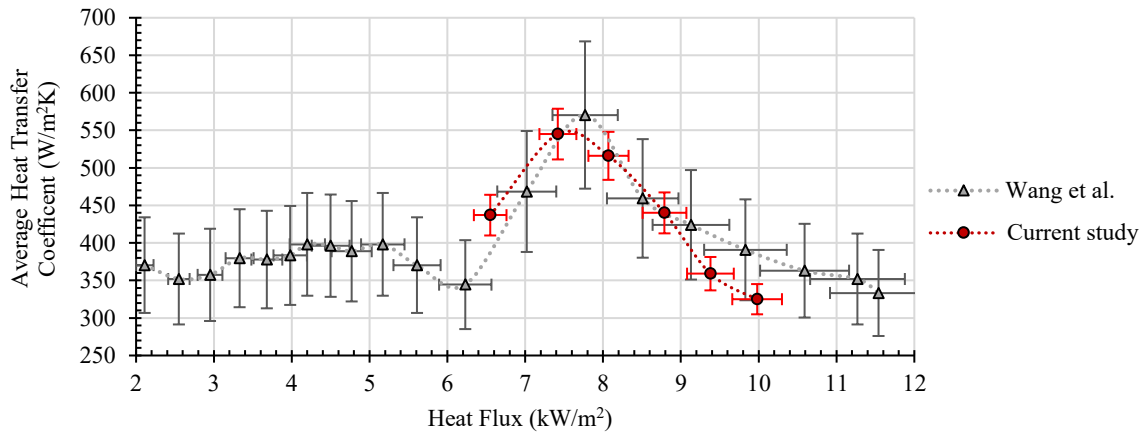
Figure 5: Experimental validation of the experimental facility with literature Wang, et al. [43]. Lines connecting the different data points are included to illustrate the trend

5.2 Instability classification

General observations of flow instability are presented next using high-speed images, surface temperature profiles and the pressure response at the inlet and outlet. Each analysis presents flow observations from the high-speed image analysis, surface temperature variability, the instability frequency, and the average period of an instability event from the pressure measurements.

During all of the flow-boiling experiments, there was a single-phase subcooled liquid region at the inlet of the channel, a nucleation site, and a vapour slug towards the outlet of the channel. Flow instability periods were associated with deviations in the flow pattern from the typical form, which also resulted in a change in the heated surface temperature. Definite starting and termination times of these periods could be observed. The start was defined when the flow pattern changed from its quasi-steady-state form, while the termination time was when the flow returned to the pre-instability form. During a typical experiment several instability occurrences might have been present. Because the periods of instability were relatively short compared to the time span of each experiment, it was possible to clearly identify the presence of an instability occurrence. For purposes of discussion in this article, three instability types were defined based on observations: phase-mixing, minor reverse flow, and major reverse flow.

Consider Figure 6 of a typical phase-mixing occurrence. For demonstration purposes this example case is selected for an arbitrary heat flux condition at a mass flux of $G = 40$ kg/m^{2}s and $\theta = 0°$ (horizontal heated surface from the bottom). Three high-speed image snapshots (a to c) at different time instances are included with corresponding thermal images given in Figure 7. Infrared images were taken at a frequency of around 25 Hz which corresponds to an image every 40 ms. This is why Figure 7 (b) is not at 10 ms but rather at 40 ms. In each image the locations of the inlet liquid region, the nucleation site, the vapour front, the two-phase region, and the regions where phase mixing occurs are highlighted in shaded blue. The phase-boundary between liquid and vapour is visible as a white edge around the vapour. Under quasi-steady state conditions, the length-wise vapour boundary remained relatively stable and well defined. Figure 6 (a) gives the flow distribution just before the instability occurred with Figure 7 (a) showing the hottest part of the channel in the two-phase region. During phase mixing (Figure 6 (b)), the vapour interior experienced liquid stream ingression and several erratically positioned liquid-vapour interfaces were visible (shown by blue highlights). The cooling effect from this instability event was small with the size of the white spot in Figure 7 (b) of similar size to that of Figure 7 (a). Typically, the mixing occurrence was initiated relatively close to the nucleation site, followed by a rapid motion of the mixing region downstream. This region could traverse the whole vapour slug length in less than 10 milliseconds and typically spanned the width of the channel, and at any one moment occupied less than 10% (less than 8 mm) of the heated length. After some time (for example 130 ms in this case) the flow returned to the pre-instability form (Figure 6 (c)). At all times the nucleation site and vapour front location remained relatively fixed and varied by less than 1% of the channel's heated length.
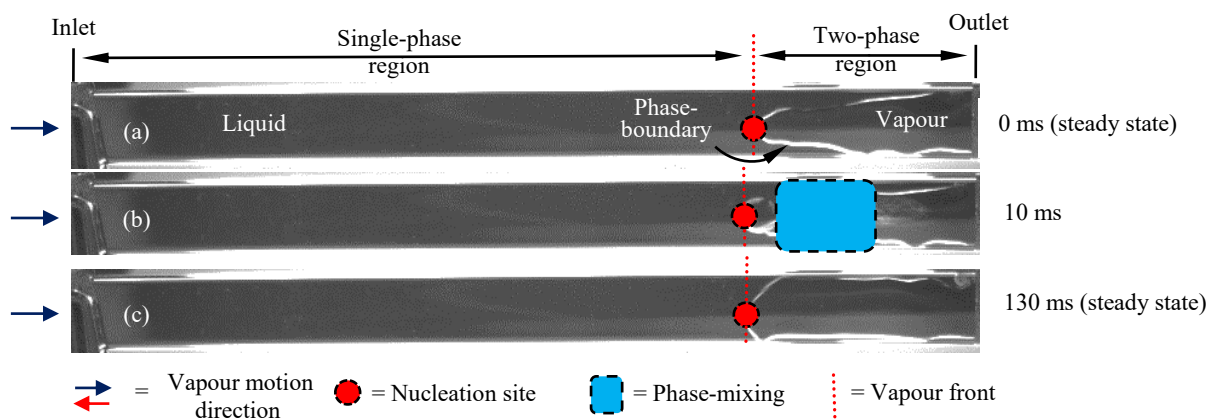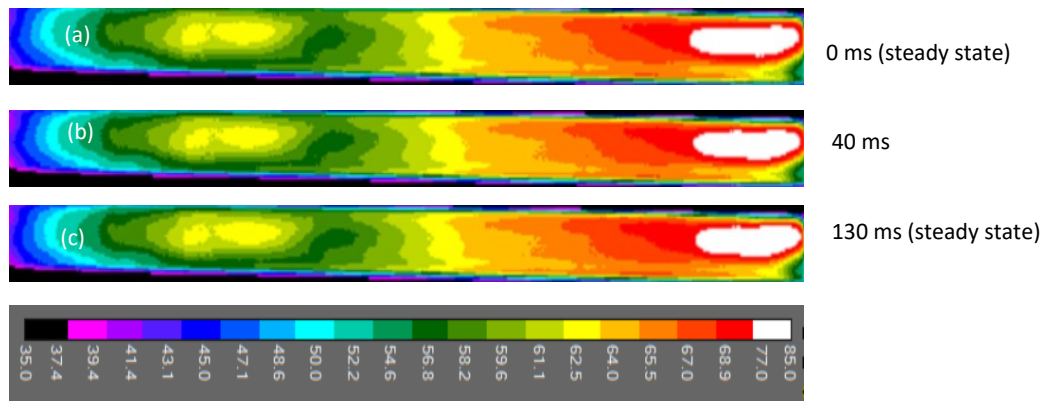
Figure 7: Infra-red images of a phase-mixing occurrence at a rotation of $\theta = 0°$, mass flux of 40 kg/m²s and heat flux of 13.6 kW/m² at three-time instances. Note: a temperature bar is supplied

The relative placement of the nucleation site and/or the vapour front was another clear indicator of the presence of a flow instability occurrence. The typical progression of a minor reverse flow disturbance is depicted in Figure 8 with highspeed images and with thermal images in Figure 9. Again, this example case is selected for demonstration purposes only at some arbitrary heat flux condition at a mass flux of $G = 40$ kg/m²s and $\theta = 0°$. During minor reverse flow disturbances, noteworthy vapour front motion towards the inlet occurred and spanned between 1% and 10% of the heated length (for purposes of this article the 10% value was based on the pressure response data which will be discussed later). In the shown example, the initial steady state flow form is given in Figure 8 (a) just before the instability started. During their initial stages, reverse flow disturbances are characterised by phase-mixing (indicated by blue in Figure 8 (b)) and a slight movement of the wave front towards the inlet. Thereafter, a significant change of the vapour front location is typically noticed, which in this example reached a maximum upstream displacement of 7% of the channel's heated length within a period of approximately 50 ms (Figure 8 (c)). During the retreat of the vapour front, phase mixing is prevalent (Figure 8 (d)). After some time, the flow form returns to the initial condition (Figure 8 (e)). For this example, the entire instability disturbance occurred within 200 ms. Changes in the infrared camera images in Figure 9 (a) to (d), are more difficult to identify due to the relatively small temperature improvement observed at different intervals of time. Nonetheless, a further analysis of the temperature profiles in Figure 22 provide an easier way to understand the influence of flow instabilities on these thermal gradients. A full discussion on the temperature improvements are given in more detail in Section 5.7 Thermal response to instability events. It can however be observed that high temperature areas in the range of 72 °C to 73.6 °C and represented in dark red, reduce during the instability event.
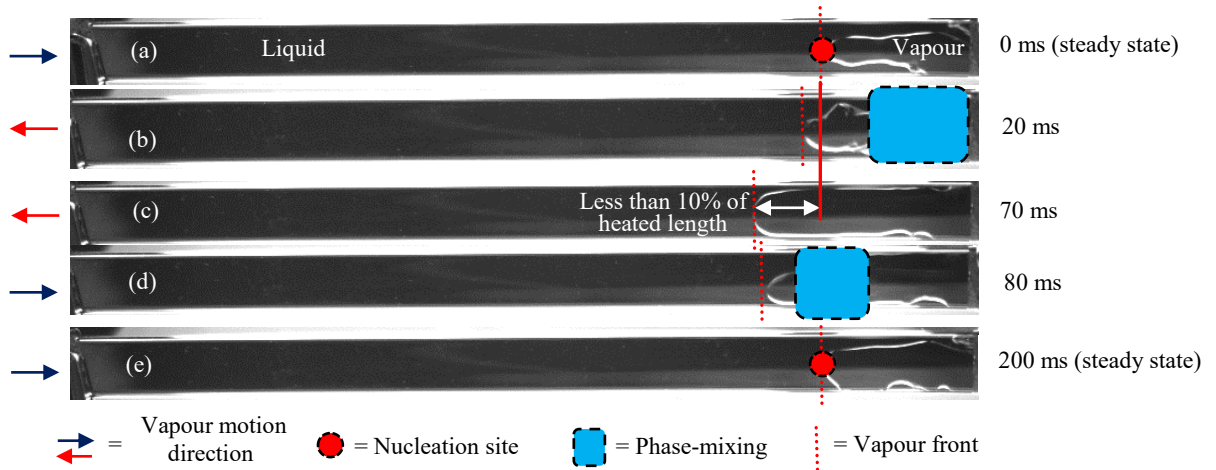
Figure 8: High-speed images of a minor reverse flow occurrence at $\theta = 0°$, mass flux at a mas flux 40 kg/m²s and heat flux of 13.6 kW/m² at various time instances. Note that the width of the channel is 5 mm to be regarded as the scale bar
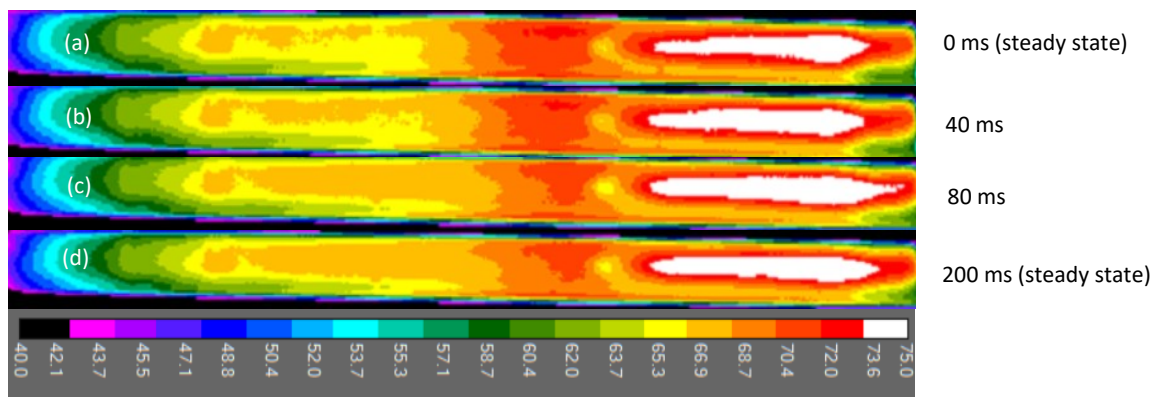

Figure 9: Infra-red images of a minor reverse flow occurrence at $\theta = 0°$, mass flux at a mas flux 40 kg/m²s and heat flux of 13.6 kW/m² at various time instances. Note: a temperature bar is supplied

For cases where the vapour front moved upstream by more than 10% of the heated length, the instability was classified as being a major reverse flow occurrence. Figure 10 shows some carefully selected high-speed image snap shots with which to explain the typical progression of such a disturbance. Again, for demonstration purposes for an arbitrary heat flux condition at a mass flux of $G = 40$ kg/m²s and $\theta = 0°$ is considered here.
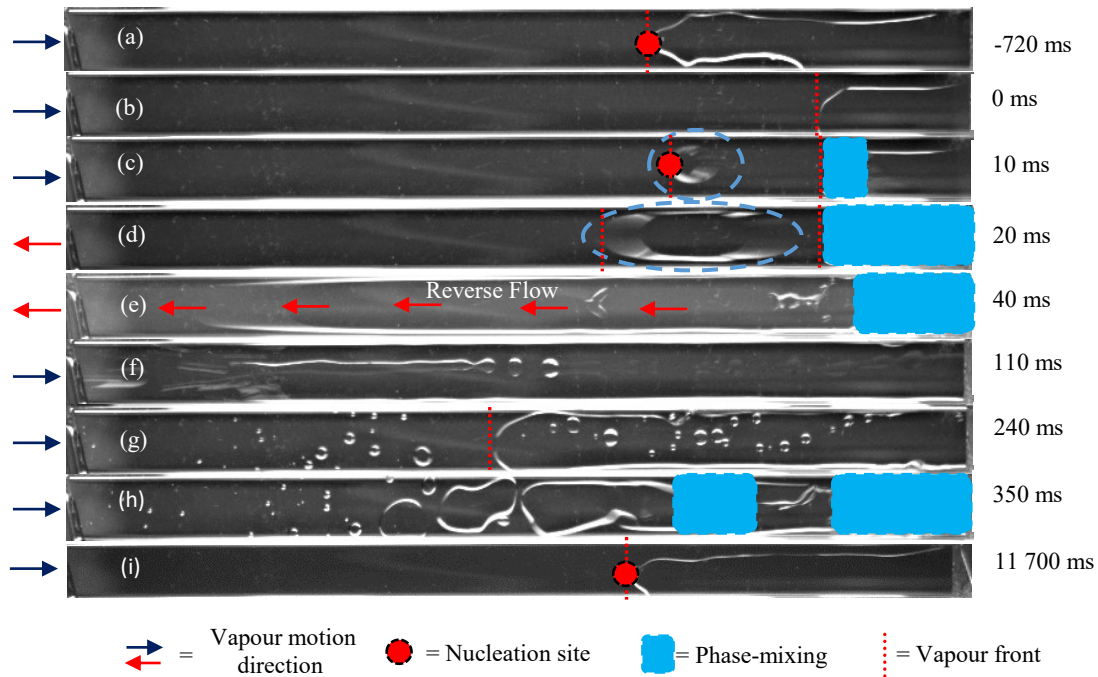
Figure 10: High-speed images of a major reverse flow occurrence at a rotation of $\theta = 0°$, mass flux of $G = 20$ m²/s and heat flux 8.2 kW/m². Note that the width of the channel is 5 mm to be regarded as the scale bar
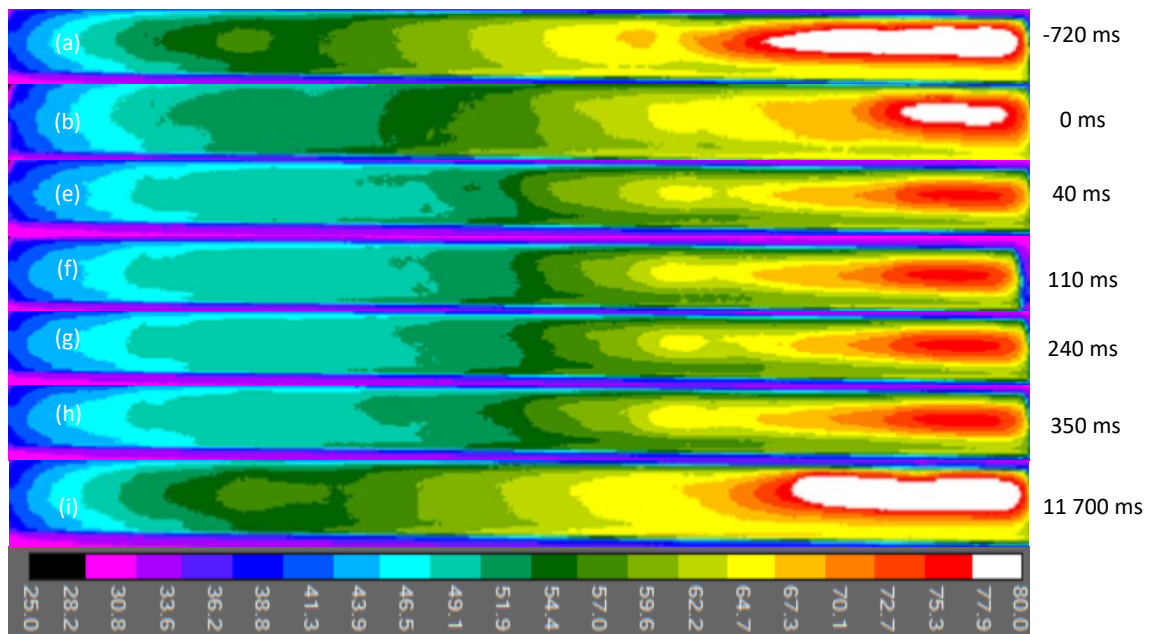

Figure 11: Infra-red images of a major reverse flow occurrence at a rotation of $\theta = 0°$, mass flux of $G = 20$ m²/s and heat flux 8.2 kW/m². Note: a temperature bar is supplied

Figure 10 (a) shows the steady state condition directly before the disturbance. During its first stage, the instability is characterised by a significant movement of the vapour front towards the outlet (Figure 10 (b)) which temporarily results in no bubble formation at the original nucleation site location. Shortly thereafter a second bubble is produced at the original nucleation site location (Figure 10 (c)) which rapidly expands in both the upstream and downstream directions (Figure 10 (d)). At the same time a phase-mixing region is initiated within

the first bubble column which is making its way towards the outlet. The upstream bubble continues to expand and can in severe cases reach the inlet of the test section as indicated in Figure 10 (e) for this example case. Typically, the vapour motion at this stage is so rapid that even with the frame rate setting of 140 fps on the camera it is not possibly to clearly distinguish whether the vapour is contained in a single large vapour slug or in multiple bubbles. From Figure 10 (f) it appears as though the vapour is spread axially along the centre of the channel as it re-enters the microchannel. Figure 10 (g) shows a large vapour slug having formed with multiple bubble upstream of the vapour front. These bubbles expanded and coalesced before attaching to the vapour front, as is shown in Figure 10 (h). The reattachment of the larger bubbles resulted in phase mixing occurring as two bubbles attached consecutively, both of which resulted in independent phase mixing. The flow boiling continued to have upstream bubbles slowly moving downstream and attaching to the main vapour slug. This process took more than 11 s to complete before a typical steady state flow form was reached as shown in Figure 10 (i). The thermal images show a clear effect of instability with the temperature in the channel decreasing substantially due to flow instability. This is identified with the size of the hottest white spot decreasing in size between images as well as the increase in turquoise in the first half of the channel. The largest change in temperature happens in the first 40 ms seconds during the initial change from steady state conditions. The temperature profile returns to a profile similar to the starting one after 11700 ms. Temperature profiles of the infrared images are presented in Figure 23 where the changes in temperature are discussed in more detail.

The cases in Figure 6, Figure 8 and Figure 10 were carefully selected to best represented the different instability types. All the instability occurrences (except major reverse flow) typically lasted less than 400 ms. This duration is important for the heat transfer coefficient improvement analysis presented later.

5.3 *Flow instability maps*

The recorded video footage during each experiment (60 s in length) for each of the experimental test cases were analysed to identify under which conditions the different flow instability types occurred. The results are presented in Figure 12 in the form of flow instability maps, at a mass flux of (a) 10 kg/m^{2}s, (b) 20 kg/m^{2}s and (c) 40 kg/m^{2}s. The prevalence of at least one occurrence of each instability type is indicated in terms of the heat flux (vertical axis) and the azimuth orientation, θ (horizontal axis) as follows: major reverse flow is indicated with red markers, minor reverse flow with yellow markers, and cases without any reverse flow occurrences with green markers. Overlaid on this is the presence of phase-mixing: markers with black fill indicates that phase mixing was present, while unfilled markers indicate the absence of phase mixing.
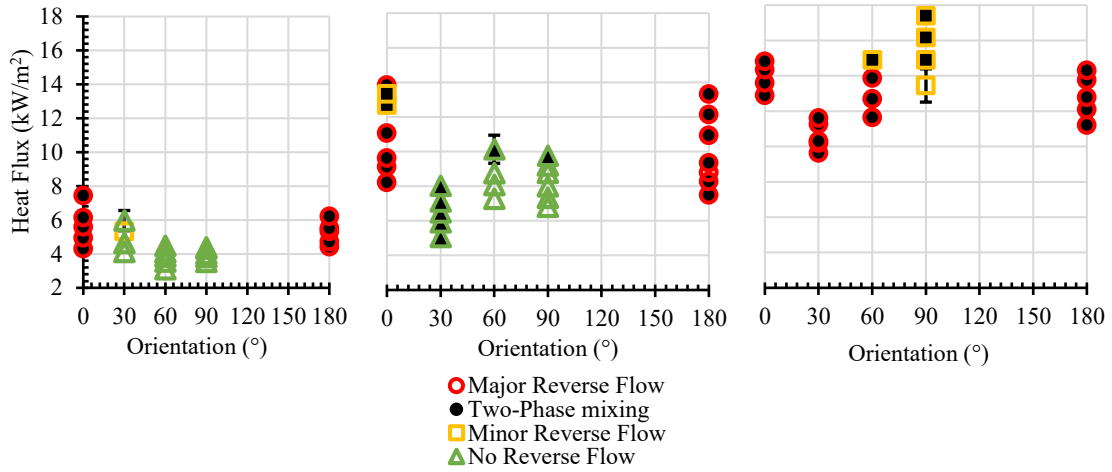
Figure 12: Flow instability maps at orientation of θ = 0°, 30°, 60°, 90° and 180° at a mass flux of (a) 10 kg/m²s, (b) 20 kg/m²s and (c) 40 kg/m²s at various heat fluxes

From the analysis it was found that in all cases, if major reverse occurrences were present within the experiment, both minor reverse occurrences and phase-mixing occurrences were present. As such, for these cases in Figure 12 only the most severe instability, namely major reverse flow is plotted. It was observed that for the parameter ranges considered in this study that the prevalence of the instability type depends strongly on θ and the mass flux, and to a lesser extent on the heat flux. Almost all the test cases with θ = 0° and 180° (horizontal bottom and top heating) exhibited major reverse flow. This suggests that the instability behaviour for these azimuth rotational orientations were independent of heat flux and mass flux. Azimuth orientations of 30°, 60°, and 90° were less likely to exhibit flow instability. As the mass flux in these cases increase, so did the prevalence of the flow instability. At the lowest mass flux of 10 kg/m²s, no instability was observed, except in one case which exhibited minor reverse flow. At a mass flux of 20 kg/m²s, no reverse flow was observed but approximately half of the cases exhibited phase mixing instabilities with θ = 60° and 90° having some heat flux effect where the highest heat fluxes tested had two-phase mixing events. This heat flux effect was again observed at a rotation of θ = 90° with all but the lowest heat flux experiencing both minor reverse flow and two-phase mixing. At 40 kg/m²s all cases exhibited reverse flow and approximately half exhibited as least one reverse flow occurrence. Based on the distribution of the filled markers in Figure 12, rudimentary indications suggest that phase mixing increases with heat flux, and/or as the heated surface approaches a horizontal azimuth orientation. Judging by the placement of the red markers, particularly in Figure 12 (c), it also seems as though a more horizontally inclined channel is more susceptible to major reverse flow instability.

5.4 Instability mechanism

Three instability events have been identified and the associated decreases in the surface temperature with these instabilities are described in Section 5.2. The mechanism causing instability events as well as the decrease in surface temperature are discussed in this section. An important consideration for instability is the confinement of the vapour in the width of the channel, as well as upstream bubble coalescence with the vapour slug within the channel. Confinement is when vapour within the channel cannot expand outwards in the width of the channel, for

example, a bottom heated channel is confined by the width of the channel while a side heated channel (θ = 90°) is confined in the depth of the channel. Horizontal channels thus, require a larger vapour volume than intermediate rotations to be confined. Unconfined vapour slugs was more likely to experience instability. When vapour slugs detach from the side walls, liquid can move between the side wall and vapour, possibly resulting in rapid phase change which would produce local increase in pressure. This is particularly true for top heated and intermediate rotations where the vapour is often directly in contact with the heated surface resulting in relatively poor heat transfer and elevated surface temperatures. Liquid encountering this elevated surface temperature would change phase rapidly causing a localised increase in pressure. These local increases in pressure have been investigated in literature to identify the role pressure plays in flow instability with one of the most important papers being that of Kandlikar [44] where instability mitigation techniques are also discussed. The instability maps presented in Section 5.3 showed that intermediate rotations were only unstable at the highest mass flux while horizontal channels were unstable at all rotations. Easier confinement of the vapour at intermediate rotations is expected to be the primary cause of the stable flow at low mass fluxes. The sudden increase in instability types at a mass flux of 40 kg/m^{2}s for intermediate rotations, was due to the increased liquid velocity at higher mass fluxes, allowing for a greater possibility that some of the liquid would get between the heated surface and vapour slug, unconfining the slug and possibly initiating an instability event.

Bubbles initially present upstream of the main vapour in the channel could also result in an instability event due to the rapid pressure release during coalescence with the main vapour slug. This was observed in Figure 10 and Figure 11 where the upstream bubbles prevented stable nucleate boiling with repeated instability events occurring in quick succession. Similar observations have been made by other authors at mass fluxes over 400 kg/m^{2}s [45]. Bubbles that form at nucleation sites have high local pressures [44] which are released once they coalesce with the large vapour slug and can result in turbulent flow. The direction in which the pressure is released determines if a two-phase mixing event or reverse flow event occurs with nucleation site location playing an important, also observed by Kandlikar [44]. The nucleation sites for the two-phase mixing event (Figure 6) and minor reverse flow event (Figure 8) are close to the exit of the channel while the nucleation site causing the major reverse flow event is closer to the inlet (Figure 10). The fluid resistance to reverse flow is greater if the nucleation site is close to the exit of the channel. Upstream bubbles could be caused by the vapour slug attaching to a nucleation site further downstream as is shown in Figure 13 (b) or a reverse flow event that causes the vapour column to break up and leave some bubble upstream, also observed in (Figure 10). Figure 13 (b) shows two active nucleation sites with a clear break between a large upstream bubble and the main vapour slug. As the upstream bubble attaches to the vapour slug, the pressure release produces two-phase mixing, and the nucleation site's location is relatively close to the inlet, resulting in reverse flow occurring, as is shown Figure 13 (c) to (e). The system returns to stability in Figure 13 (f) but is likely to have another instability event soon due to the large upstream bubbles forming before attaching to the vapour in the channel. These upstream bubbles are however much smaller than the one in Figure 13 (b) which caused the major reverse flow observed.
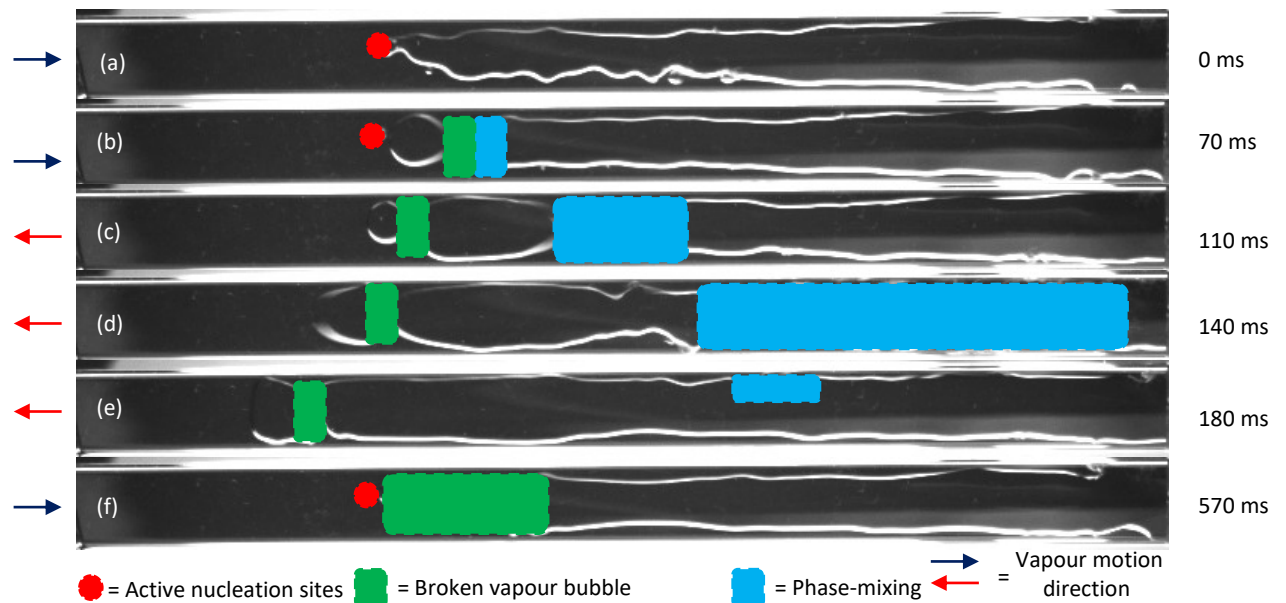
Figure 13: Major reverse flow due to vapour bubble break up at a mass flux of 40 kg/m²s, rotation of 0° and heat flux of 13.6 kW/m²

Coalescence of upstream bubbles to the main vapour slug don't always cause reverse flow, two-phase mixing only can also occur as is shown in Figure 14. The upstream bubbles in Figure 14 (a) coalesce together and then to the main vapour slug and result in a two-phase mixing event. The prevalence, frequency and cooling effect of each instability type will be further discussed in the sections that follow.
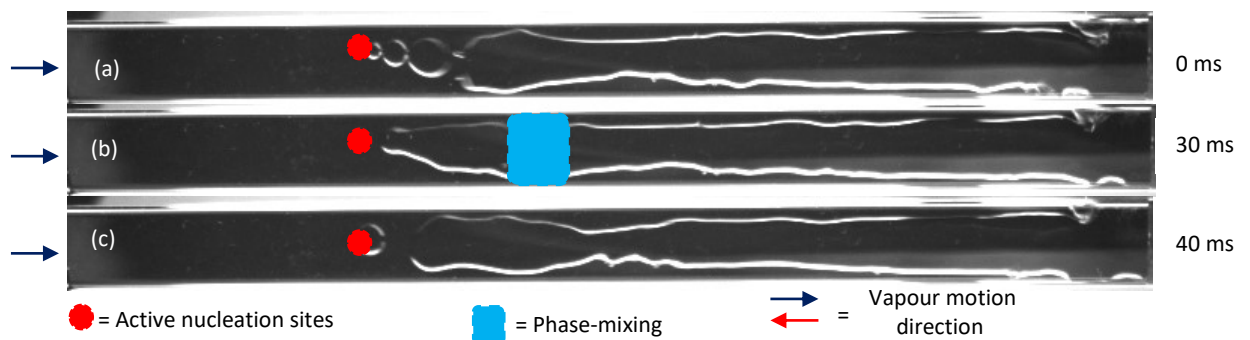
Figure 14: Two-phase mixing event due to vapour bubble break up at a mass flux of 40 kg/m²s, rotation of 0° and heat flux of 13.6 kW/m²

Stable boiling is associated with low fluid velocities due to the low mass fluxes tested. Laminar flow regimes results (approximately $14 \leq Re \leq 57$) in the channel having large temperature gradients due to buoyancy at intermediate rotations. In Figure 15 a channel at a rotation of $\theta = 60°$ at an arbitrary mass flux and heat flux shows a stable highspeed (a) and infrared images (c) and corresponding highspeed (b) and infrared image (d) after a two-phase mixing event occurred. In both cases, the vapour and hot liquid move to the top of the channel while the colder liquid remains at the bottom of the channel, producing temperature gradients of more than 50°C in the two-phase region. The two-phase mixing event that occurs near the inlet of the channel, shown in Figure 15 (b), results in a decrease in the surface temperature at the same location in Figure 15 (d) where the size of the dark green (approximately 78°C) reduces to turquoise (around 66°C). This decrease in the temperature reduces the average surface temperature in the cross section and improves the heat transfer coefficient.
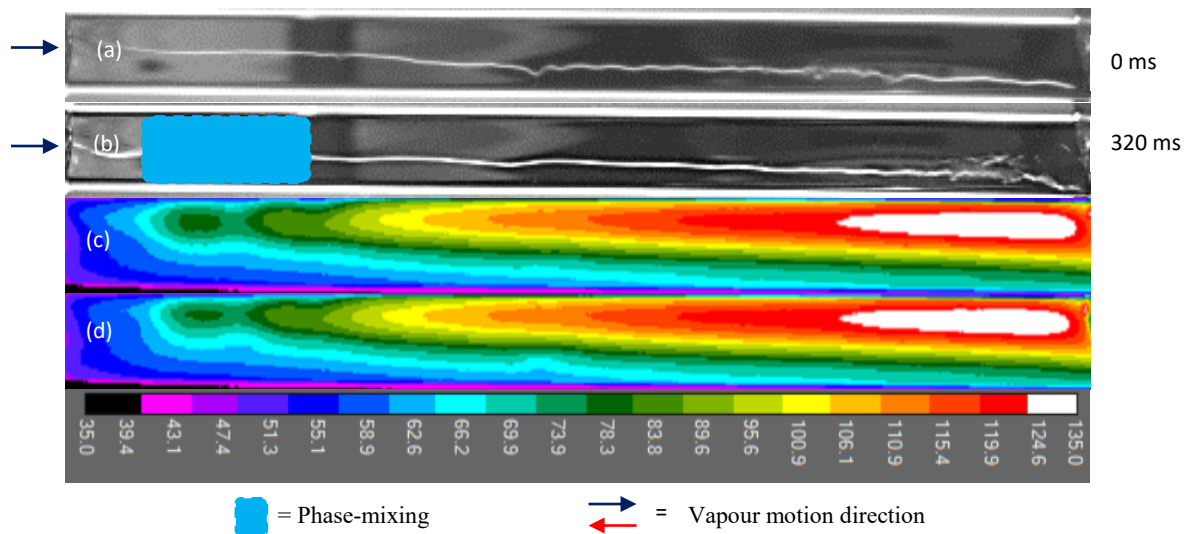
24

Figure 15: Two-phase mixing event effect on the large thermal gradient of a channel at a rotation of $\theta = 60°$

Instability causes decreases in temperature due to the high temperature vapour in contact with the heated surface being replaced by liquid. This liquid replacing the vapour increased the heat transfer due to the thermal conductivity of the liquid being higher than that of the vapour and the lower temperature of the liquid. The increased fluid velocity also aids to decrease the surface temperature by replacing the local fluid at a temperature close to that of the surface with cooler mixed liquid and vapour.

5.5 Pressure response of instability events

In addition to the flow visualization, the pressure response at the inlet and the outlet of the test section was also carefully scrutinised. It was found that each type of flow instability (phase-mixing, minor reverse flow, and major reverse flow) corresponded with a particular pressure response. As mentioned previously, pressure readings were sampled at 100 Hz which was found to be a sufficient resolution to monitor the transient pressure responses during flow instability periods. Pressure readings varied either due to the prevailing flow phenomena (such as instability) or natural variations from sources such as system noise. Flow change phenomena typically resulted in substantial changes in the surface temperature while natural variations were inconsequential in terms of surface temperatures. Differentiating between the cause of the variation was essential. For this purpose, readings were compared to the mean pressure reading over the duration of each experiment. Natural variations and system noise resulted in significantly smaller deviations than during periods of flow instability.

A threshold deviation magnitude was used to identify the occurrence of flow instability periods. The same selected threshold value was applied to all test cases irrespective of θ, the mass flux and heat flux; and was obtained in conjunction with the flow visualization analysis of the previous section. Mass and heat flux cases that had neither reverse flow nor phase-mixing occurrences were used to calibrate the instability threshold. If the instability threshold value is too large, it would not be able capture low magnitude instability events, whereas it the instability threshold is too low, it would label natural variation in pressure as instability events while there might not be occurrence of flow instabilities.

A suitable threshold was obtained by considering values between 0.5 kPa and 2 kPa in increments of 0.1 kPa. The number of missed instability periods and the number of false positives were checked for each value of θ, and then minimised. Based on this, a pressure deviation threshold of 0.8 kPa was selected. This value resulted in no false positives at any θ and minor under-reporting of instability occurrences. Because flow instability was found to be beneficial for heat transfer (as will be presented later), this slight underreporting posed less of a problem than over reporting and ensured a conservative approach by guarded against the over-estimation of the heat transfer improvement. Differentiation between phase-mixing, minor reverse flow and major reverse flow occurrences was done by considering a typical inlet and outlet pressure response for the three instability types. For demonstration purposes, the pressure responses of the example cases, mentioned previously, are used here.

The inlet and outlet pressure readings (red and blue respectively) are shown in Figure 16 for the phase-mixing example of Figure 6. The outlet pressure exceeds the outlet threshold pressure at 20.34 s (measured from the start of the experiment). This time corresponds to the moment the two-phase mixing event was first observed visually. Importantly, for phase-mixing, the pressure at the inlet does not change substantially and never exceeds the inlet instability threshold pressure.
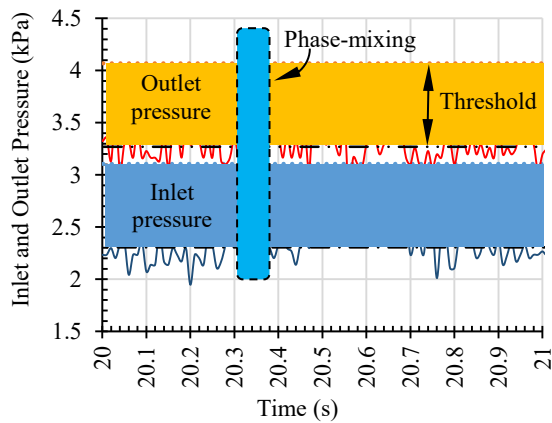

Figure 16: Pressure response for a two-phase mixing event for an arbitrary rotation, mass flux and heat flux (images shown in Figure 6**).**

The pressure readings of the minor reverse flow occurrence presented earlier in Figure 8 is shown in a similar manner in Figure 17, except that the relative pressure values above the mean pressure value is plotted. The inlet pressure exceeds the threshold at 30 s and corresponds to the 70 ms time stamp in Figure 8. In contrast to phase-mixing, for minor reverse flow occurrences the pressures at the outlet does not exceed the outlet instability threshold at any point in time.
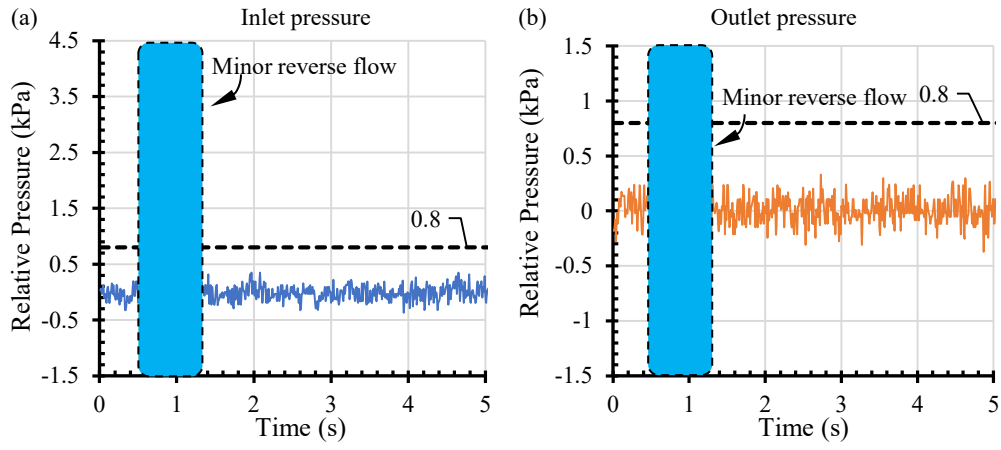
Figure 17: Relative pressure response (in terms of the mean pressure) of a minor reverse flow event for an arbitrary rotation, mass flux and heat flux at the (a) inlet and (b) outlet from experimental observations earlier reported in Figure 6

Likewise, the pressure readings of the major reverse flow example are given in Figure 18 (not plotted as a relative pressure). At the instability occurrence, both the inlet and outlet pressure breached the thresholds. The initial increase in pressure coincides with the initiation of the instability events presented in Figure 10. The time between the initial change in pressure to seemingly quasi-steady conditions was 1.3 s at the inlet and 0.02 s at the outlet.
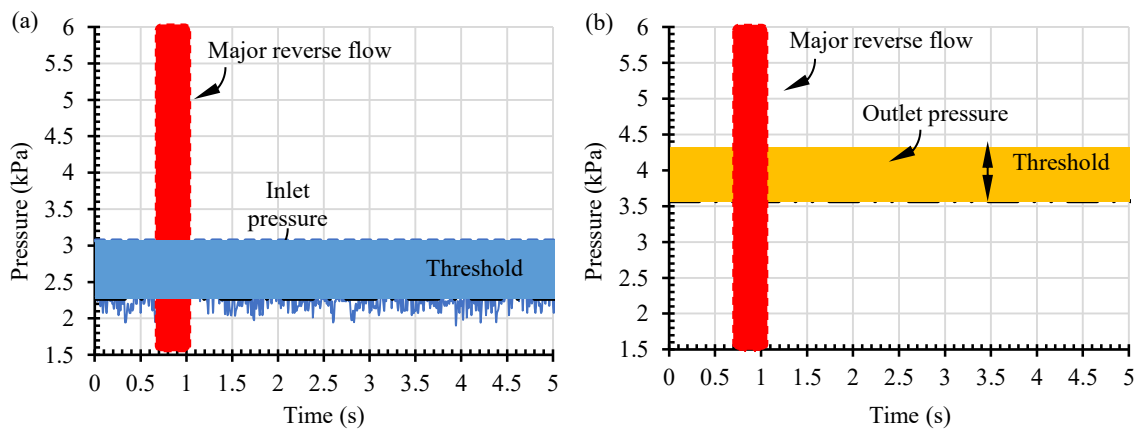

Figure 18: Pressure response of a major reverse flow event at an arbitrary rotation, mass flux and heat flux at the (a) inlet and (b) outlet from experimental observations earlier reported in Figure 11

The pressure responses for the three instability cases suggest that the inlet and outlet pressure transducers could be used to differentiate between each instability type. Phase-mixing instabilities could be identified when the outlet pressure breached the threshold, minor reverse flow instabilities when the inlet pressure breached the threshold, and major reverse flow occurrences when both the inlet and outlet pressures breached the thresholds simultaneously. Minor reverse flow events and two-phase mixing occurred could occur within 1 second of each. Thus, a major reverse flow event in this study was defined as an increase in the inlet and outlet threshold above the instability frequency within 0.2 s of each other. If the increase in pressure occurred outside of this time frame, the event would be defined as a two-phase mixing event or a minor reverse flow event.

5.6 Intensity and frequency of instability events – pressure analysis

Based on both or either of the inlet and outlet pressure readings, many test case recordings contained multiple instability periods with the experimental time span. To better report the instability prevalence, the number of instability events (n) during each experimental duration ($\Delta t = 60\ s$) was checked and its average instability occurrence frequency (f) was determined as follows:

$$f = \frac{n}{\Delta t} \tag{12}$$

Because of the high sampling rate, multiple consecutive pressure readings (taken at 100 Hz) during a single instability period would be above the threshold value. To correctly identify instability periods, these consecutive datapoints were grouped together and reported as a single instability period. Because each test condition was repeated three times, the arithmetic average frequency for each combination of θ, mass flux, and heat flux are reported here.

The phase-mixing occurrence frequencies (when they occur without reverse flow) are shown in Figure 19. Note that some frequencies on the x axis were 0 Hz, corresponding to no phase-mixing being identified. As was shown in Figure 12, only $\theta = 180°$ (horizontal heating from above) experienced isolated two-phase mixing events. The main difference in the vapour slug's position at a rotation of $\theta = 180°$ is that the vapour slug is almost completely confined during period without instability (unlike $\theta = 30°$, $60°$ and $90°$) and on the heated surface (unlike $\theta = 0°$). These two bubble positioning effects are expected to be the main cause for the two-phase mixing frequencies being higher. When liquid does make it onto the heated surface the rapid expansion could result in reverse flow or the bubble becoming unconfined producing two-phase mixing.
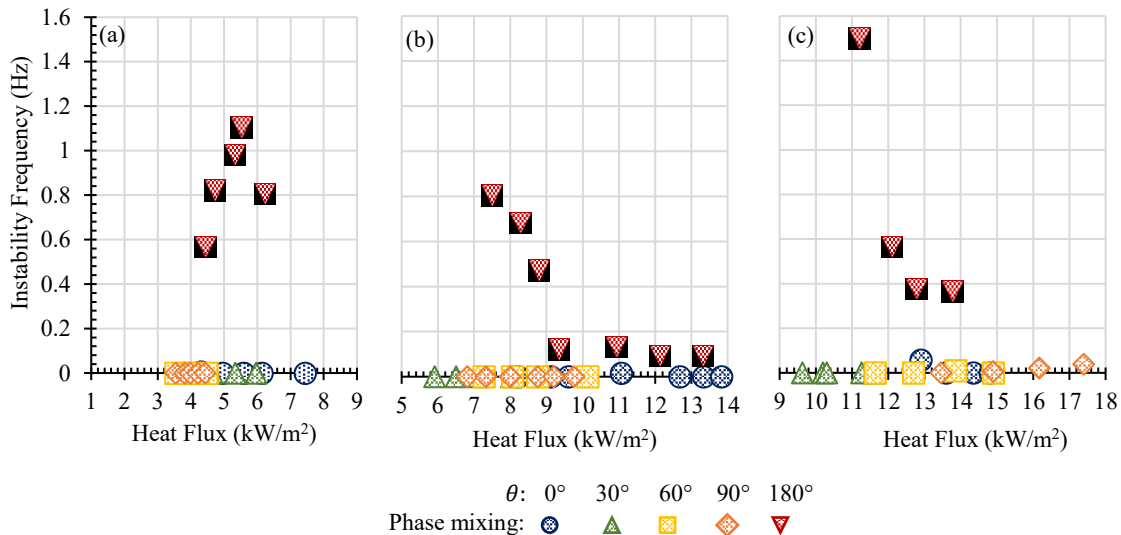

Figure 19: Phase-mixing instability frequency at a mass flux of (a) 10 kg/m²s, (b) 20 kg/m²s and (c) 40 kg/m²s. Note that values over the x-axis can adopt values of instability frequency equal 0 or close to 0.

It was found that at mass fluxes of 20 kg/m²s and 40 kg/m²s, the frequency of the isolated phase-mixing occurrences for $\theta = 180°$ decreased as heat flux increased. This decrease is probably due to the increasing vapour

slug size with an increase in heat flux. A larger vapour slug would require the liquid to penetrate further into the vapour slug, lowering the probability that the liquid would reach the heated surface and instantly vaporise, resulting a two-phase mixing event. A different trend with an initial increase and then decrease on the instability frequency with heat flux was observed at a mass flux of 10 kg/m^{2}s.

Major and minor reverse flow frequencies are presented in Figure 20. Note that as before some frequencies on the x axis were 0 Hz, corresponding to no minor or major reverse flow being identified. Once the outlet pressure breached the threshold, it was checked whether the inlet pressure also breached the threshold within 0.2 s. If it did, the occurrence was classified as major reverse flow instability, and are indicated by filled markers. Both figures show results at a mass flux of (a) 10 kg/m^{2}s, (b) 20 kg/m^{2}s and (c) 40 kg/m^{2}s.
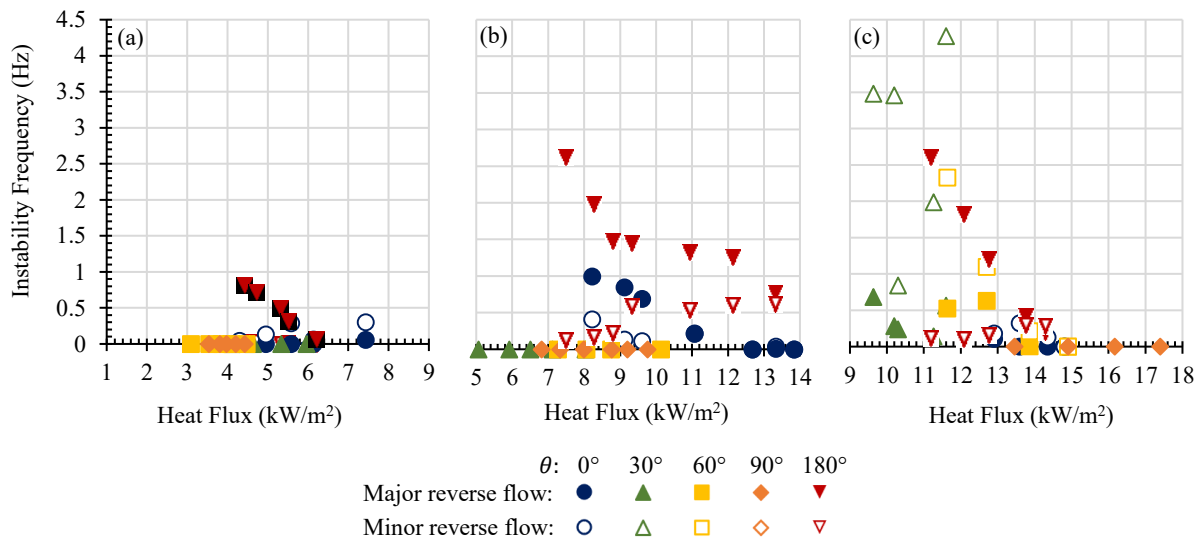

Figure 20: Major and minor reverse flow instability frequency at a mass flux of (a) 10 kg/m^{2}s, (b) 20 kg/m^{2}s and (c) 40 kg/m^{2}s

From Figure 20, it can be deduced that θ, mass flux, and heat flux have an influence on the prevalence of major and minor reverse flow instabilities. Generally, at any heat flux, $\theta = 180°$ exhibited the most flow instability. Irrespective of the mass flux, major reverse flow frequency at $\theta = 180°$ decreased as heat flux increased. It is expected that this is due to the higher vapour quality making it more difficult for liquid to penetrate through the vapour slug and larger liquid rapid expansions into vapour being required to produce the same magnitude of vapour motion towards the inlet. Conversely, the minor reverse flow frequency increased as heat flux increased at a mass flux of 20 kg/m^{2}s. Minor reverse flow frequencies were never more than 0.3 Hz at a mass flux of 10 kg/m^{2}s and 40 kg/m^{2}s. Orientation of $\theta = 30°$ and 60° had negligible instability frequencies at a mass flux of 10 kg/m^{2}s and 20 kg/m^{2}s. When the mass flux increased to 40 kg/m^{2}s a non-negligible major and minor reverse flow frequency was recorded. This mass flux effect is expected to be due to the high inertial force of the liquid being able to be penetrated the fully confined region of the vapour slug. This region typically has surface temperatures large enough to cause rapid vaporization of the liquid which would allow reverse flow to occur. The trend towards stability with an increase in the heat flux is also due to the size of the vapour slug increasing to the point where the rapid expansions of the liquid are too small compared to the size of the vapour slug to produce substantial vapour motion towards the inlet. The minor reverse flow presentation of $\theta = 30°$'s second nucleation site which became more active as heat flux increased. Note also the greater occurrence of instability events in the

29

case of $\theta = 30°$ and $60°$ in minor reverse flow when compared to major reverse flow. Cases with $\theta = 90°$ (vertical heated wall) had no major or minor reverse flow at any mass flux or heat flux combination. It is expected that this is due to near complete confinement of the vapour slug in the two-phase region at the top of the channel with all liquid passing easily underneath the bubble. It was not possible to verify this hypothesis in this study as only one highspeed camera was available. Even with two highspeed cameras it may still have been impossible to verify this without a 3D imaging technique. When $\theta = 0°$ the instability frequencies ranged from 0 Hz to 1 Hz. Cases with a mass flux of 20 kg/m²s produced the most unstable results. At this mass flux an increased heat flux resulted in a decrease in the instability frequency. At a mass flux of 10 kg/m²s an increase in the heat flux resulted in a marginal increase in the instability frequency. Additional data would be needed to determine if the increase continues.

5.7 Thermal response to instability events

Flow instability resulted in surface temperature changes. In this section, these changes are presented with the aid of temperature profiles along the length of the channel for each of the three instability types discussed previously. For this purpose, the width-wise average surface temperature along the heated length between the inlet and outlet of the channel were determined and plotted. In each case the surface temperature, before, during, and after the instability occurrence, are shown.

The temperature profiles of the two-phase mixing event previously presented in Figure 5 are shown in Figure 21. The vapour slug front was approximately 66 mm from the inlet, as indicated. The surface temperature in the vapour region decreased, resulting in an increase in the heat transfer performance. The liquid temperature in the two-phase region was defined as the saturation temperature in this study which was measured by the outlet thermocouple. The two-phase mixing event presented above had a heat transfer coefficient improvement of less than 1% in the two-phase region.
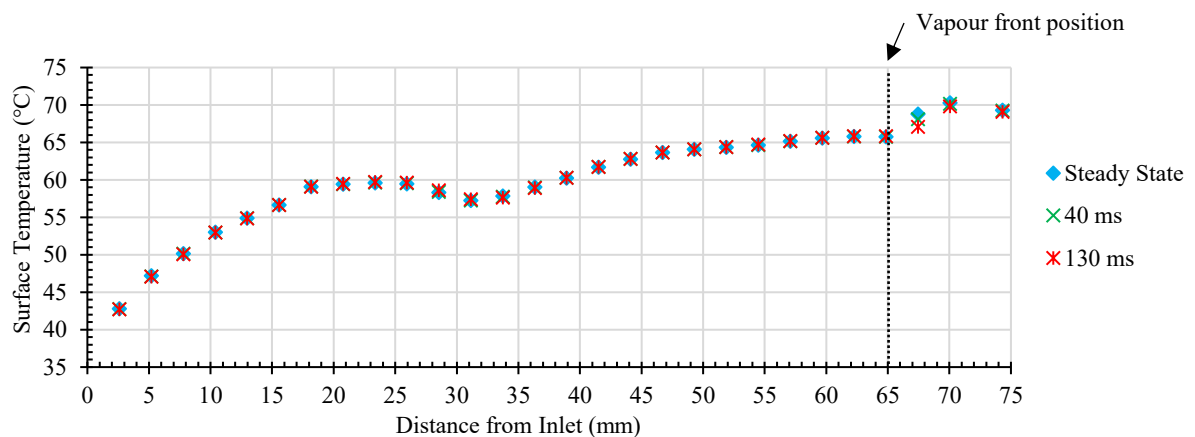

Figure 21: Average surface temperature response due to a two-phase mixing event at a $\theta = 0°$, mass flux of 40 kg/m²s and heat flux of 13.6 kW/m²

The temperature response for a minor reverse flow event is presented in Figure 22. The temperature profile had a decrease both in the single-phase region (between the vapour front position and the inlet) as well as the two-phase region (between the vapour front position and the outlet). This minor reverse flow event resulted in a surface temperature decrease in both these regions. A return to stability at 200 ms resulted in surface temperature similar

or greater than the initial steady-state profile. The average heat transfer coefficient improvement α for this example in the single-phase and two-phase region is 1.6% and 3.2% respectively. This improvement shows that minor reverse flow is marginally beneficial for heat transfer in both the single-phase and two-phase regions.
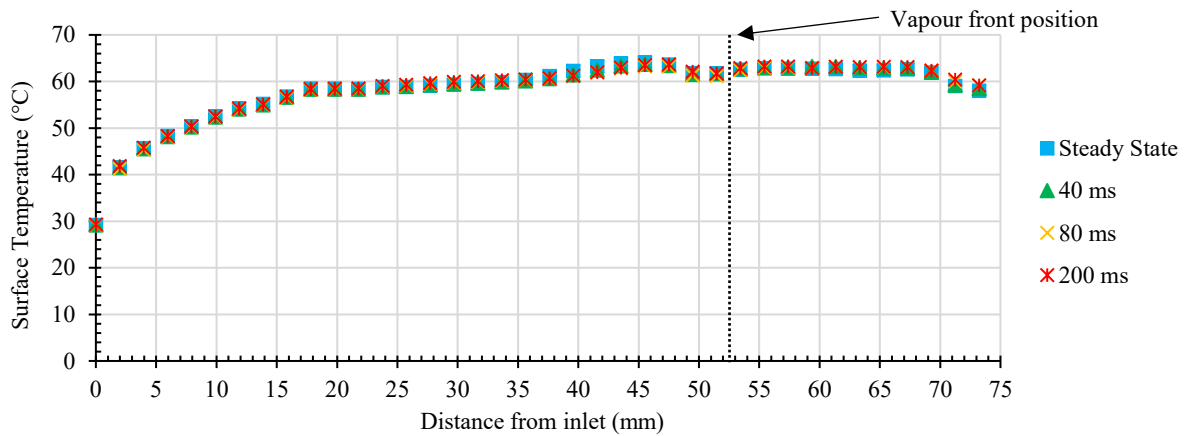

Figure 22: Average surface temperature response due to a minor reverse flow at $\theta = 0°$, mass flux of 40 kg/m²s and heat flux of 13.6 kW/m²

Surface temperature profiles for the major reverse flow event previously presented is shown in Figure 23. The temperature profiles decrease in most axial positions between the new front position and the final position after the flow instability occurred at 360 ms. The major reverse flow cases had the largest heat transfer coefficient improvement measured of all flow instability cases. In the presented example, which was the case with highest improvement in the heat transfer coefficient, the heat transfer improvement in the single-phase region was 77% and in the two-phase region was 275%. This case was selected to clearly demonstrate that severe reverse flow could be highly beneficial to the heat transfer performance. Averaged, more representative heat transfer performance improvements are presented in the next section.
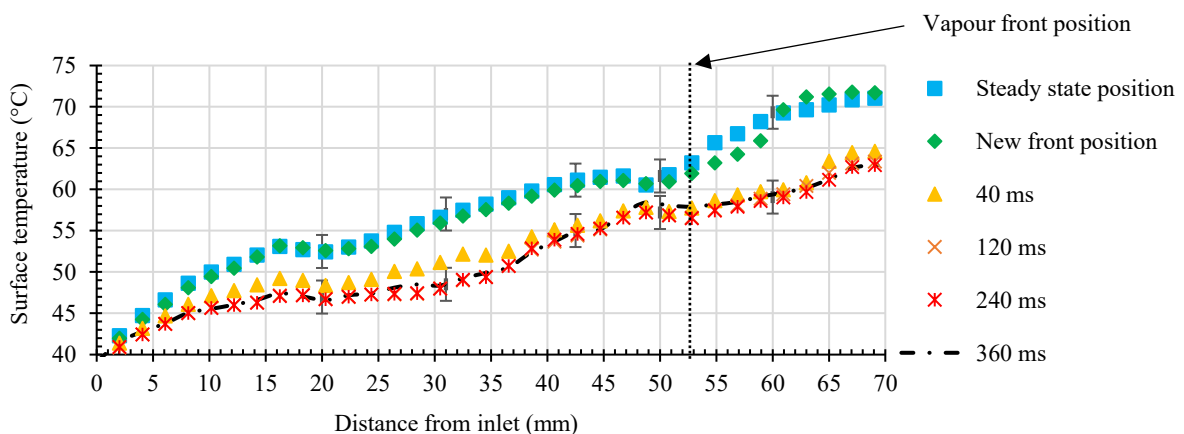

Figure 23: Average surface temperature response due to a major reverse flow event at $\theta = 0°$, mass flux of 20 m²/s and heat flux 8.2 kW/m²

5.8 Heat transfer coefficient changes

The typical heat transfer coefficient improvements α in the single-phase and two-phase region are presented in this section. The single-phase and two-phase regions were defined using the time averaged calculated vapour

quality profiles and used extensively in previous published work [46]. Each flow instability case detected (using the pressure transducers) was analysed independently. For each case, the surface temperature profile the moment before the instability, was used as the reference. The temperature profiles over the following 1 second was then compared to the reference with the lowest average surface temperature in each region taken as the maximum temperature decrease. The heat transfer coefficients of the reference and lowest surface temperature case were then calculated based on the average liquid temperature and surface temperatures. The heat transfer coefficient improvement was then determined as a percentage improvement. Time averaged local heat transfer coefficients are provided in previous published work [46]. This study considers the average improvement in the single-phase and two-phase regions so that the overall effects of the instability can be easily identified.

Heat transfer coefficients for each azimuth rotation (θ), mass flux (G) and heat flux ($\dot{q}$) combination, were grouped by the type of instability that was detected i.e., two-phase mixing, minor reverse flow, and major reverse flow as well the differentiated by the two-phase and single-phase region. At each test case 3 repetitions were completed with the average improvement of all instability cases across all three repetitions reported. These heat transfer coefficient improvement results are shown in Figure 24 (single-phase region) and Figure 25 (two-phase region) at a mass fluxes of (a) 10 kg/m²s, (b) 20 kg/m²s and (c) 40 kg/m²s. Against expectation, it was found that mixing in the two-phase region not only influences the two-phase region heat transfer coefficient, but also the heat transfer coefficient in the upstream liquid region, albeit with a smaller relative percentage magnitude.
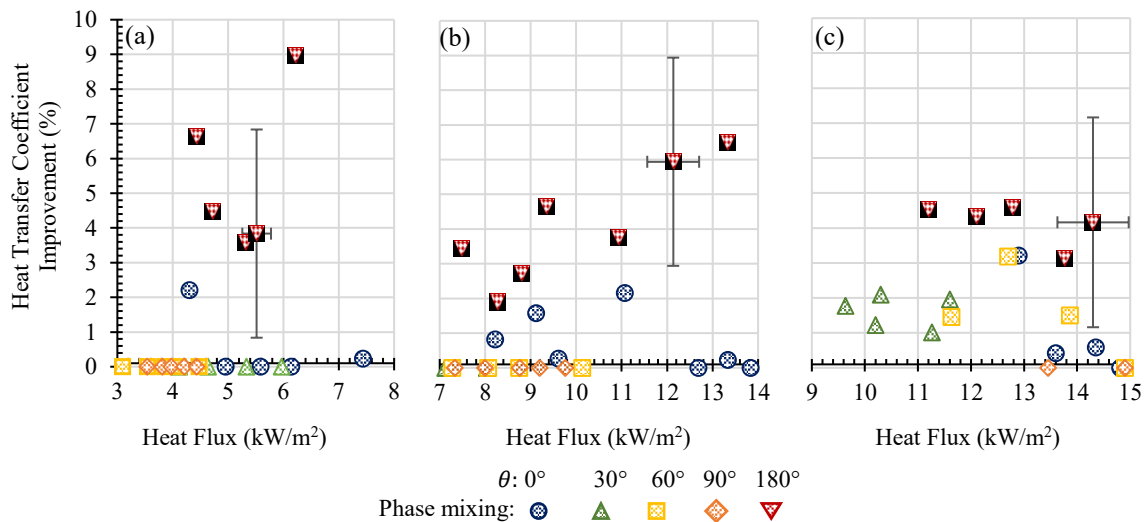

Figure 24: Average heat transfer coefficient improvement in the single-phase region due to phase-mixing instabilities at a mass flux of (a) 10 kg/m²s, (b) 20 kg/m²s and (c) 40 kg/m²s
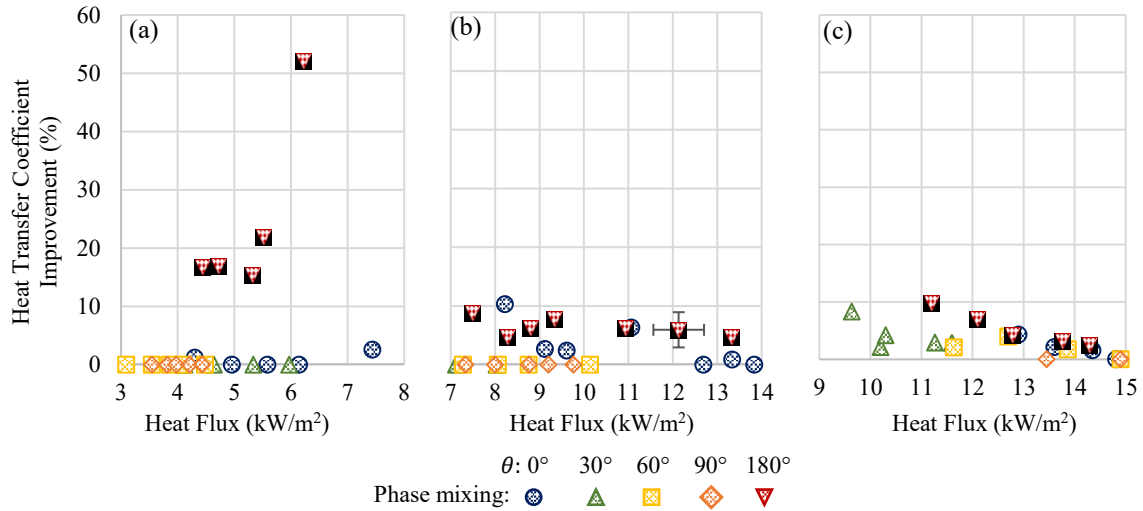
Figure 25: Average heat transfer coefficient improvement in the two-phase region due to phase-mixing instabilities at a mass flux of (a) 10 kg/m²s, (b) 20 kg/m²s and (c) 40 kg/m²s

At a mass flux of 10 kg/m²s, θ = 180° was the only rotational orientation to exhibited a substantial improvement in the heat transfer coefficient. This was expected from the instability frequency analysis where θ = 30°, 60° and 90° had negligible instability frequencies. An improvement of up to 9 % and 52% was recorded in the single and two-phase region respectively (at a heat flux of 6.2 kW/m²). θ = 0° and 180° had non-negligible heat transfer coefficient improvements at a mass flux of 20 kg/m²s within the uncertainty of the measurement. It does, however, seem that θ = 0° had some heat flux dependence with a decrease in the heat transfer coefficient improvement at higher heat fluxes. θ = 180° remained approximately constant with no substantial changes in the heat transfer coefficient with an increase in the heat flux. It is important to note that the maximum average heat transfer coefficient improvement is 5 times higher at a mass flux of 10 kg/m²s than at a mass flux of 20 kg/m²s. The maximum heat transfer coefficient improvement at a mass flux of 40 kg/m²s was approximately the same as at a mass flux of 20 kg/m²s, at around 10%. At 40 kg/m²s, θ = 90° was the only rotation orientation to exhibit a negligible instability frequency, and therefore a negligible heat transfer coefficient improvement. θ = 0° and 60° have a heat flux influence with a decrease in the heat transfer coefficient as heat flux increases. θ = 30° and 180° had no appreciable heat flux effect.

The heat transfer coefficients improvements due to minor reverse flow are presented in Figure 26. Here the single-phase and two-phase data are plotted together. As before, the heat transfer coefficient improvement is relative to the temperature profile the moment before each instability event. The improvement presented is the average heat transfer coefficient improvement from all instability events recorded at each test condition.
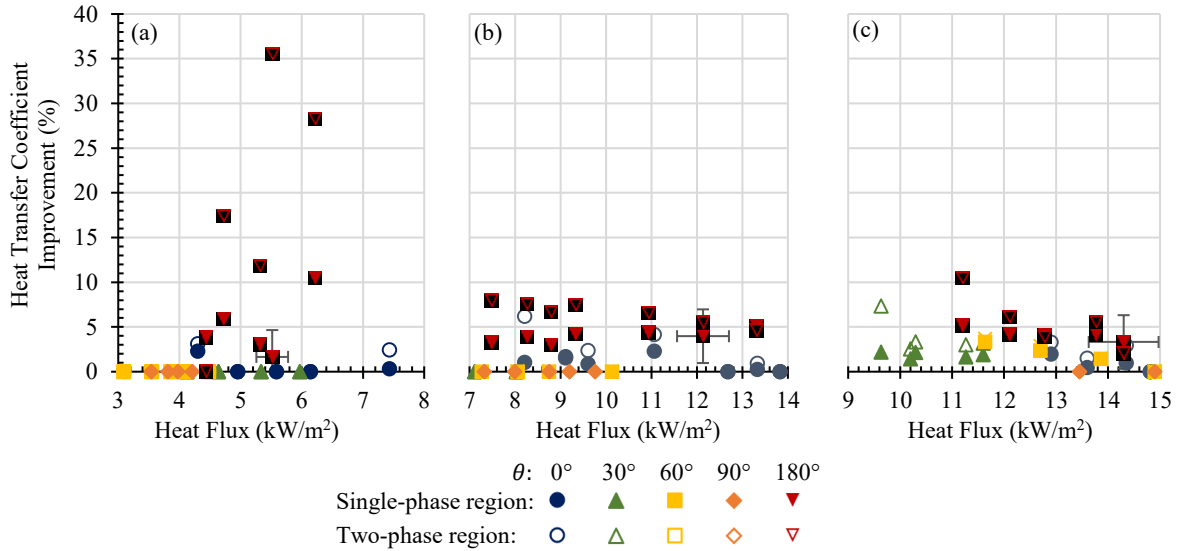
Figure 26: Average heat transfer coefficient improvement due to minor reverse flow events in the single-phase and two-phase region at a mass flux of (a) 10 kg/m²s, (b) 20 kg/m²s and (c) 40 kg/m²s

The heat transfer coefficient improvements in Figure 26 were either positive or zero. In the case where the improvement was zero, this was due to no minor reverse flow being recorded. $\theta = 90°$ for example, had no minor reverse flow event recorded by the pressure transducers at any mass flux, resulting in no heat transfer coefficient improvement show in Figure 26 (a), (b) or (c). All minor reverse flow events resulted in recorded improvement. The heat transfer coefficient improvement in the two-phase region was typically higher than the improvement in the single-phase at the same rotation, mass flux and heat flux. The increased heat transfer coefficient improvement in the two-phase region is expected to be due to vapour in the two-phase region producing a lower heat transfer coefficient during steady state conditions. Thus, any bubble dynamic effect that would improve the heat transfer would have a greater effect in the two-phase region.

The number rotations and heat flux cases with non-zero heat transfer coefficients increased as increased as mass flux increased. Only $\theta = 180°$ had non-zero heat transfer coefficients at a mass flux of 10 kg/m²s. $\theta = 0°$ had non-zero heat transfer coefficients at a heat flux of 4.3 kW/m² and 7.4 kW/m² but they were within the measurement error. $\theta = 0°$ and 180° both had non-zero heat transfer coefficient improvements at a mass flux of 20 kg/m²s. At the highest mass flux tested (40 kg/m²s), $\theta = 0°$, 30°, 60° and 180° had non-zero heat transfer coefficient improvements.

At a mass flux of 10 kg/m²s, the maximum heat transfer coefficient improvement was up to 35% in the two-phase region at a rotation of $\theta = 180°$, which is in agreement with the work of Li et al. [27]. This improvement was up to 250% higher than the maximum improvement of 8% and 10% at a mass flux of 20 kg/m²s and 40 kg/m²s. All heat transfer coefficient improvements at a heat flux greater than 4.4 kW/m² in the two-phase region of $\theta = 180°$ was more than the maximum heat transfer coefficient improvements at a mass flux of 20 kg/m²s and 40 kg/m²s. It is expected this is because the effect of vapour on the heated wall at the 10 kg/m²s was more pronounced, allowing a greater improvement to be achieved. At a mass flux of 10 kg/m²s, the liquid would have less momentum and could find it more difficult to come between the vapour slug and the heated wall. This would result in a lower heat transfer coefficient due to the high surface temperature from the near dryout conditions. At a mass flux of 20 kg/m²s and 40 kg/m²s the momentum of the fluid is greater allowing the liquid to come between

the vapour slug and heated wall more easily producing a higher steady-state heat transfer coefficient leaving less room for an improvement to occur.

No clear consistent heat flux effect is observed in Figure 26 (a), (b) or (c). A mass flux of 10 kg/m²s had some increase in the heat transfer coefficient improvement as heat flux increased in the two-phase region at a rotation of $\theta = 180°$. A decline from 8% to 4.6% was observed at a mass flux of 20 kg/m²s in the two-phase region at a rotation of $\theta = 180°$ as heat flux increased. Similarly, $\theta = 0°$ had a decrease in the heat transfer coefficient improvement in the single-phase and two-phase region as heat flux increased. $\theta = 0°$, 60° and 180° had a decline in the heat transfer coefficient improvement as heat flux increased at a mass flux of 40 kg/m²s. $\theta = 30°$ stayed more consistent as heat flux increased, it is expected that the secondary nucleation site was the reason for this, the effect of this nucleation site is discussed in previous published work [46].

Major reverse flow instabilities had a substantial effect on the heat transfer coefficient improvement, as shown in Figure 27. Some orientation, mass flux and heat flux combination had no minor reverse flow occurring. IN those cases, the heat transfer improvement was represented as zero in Figure 27 below. In all cases where a major reverse flow event was detected by the pressure transducers, this instability event produced a positive heat transfer coefficient improvement.
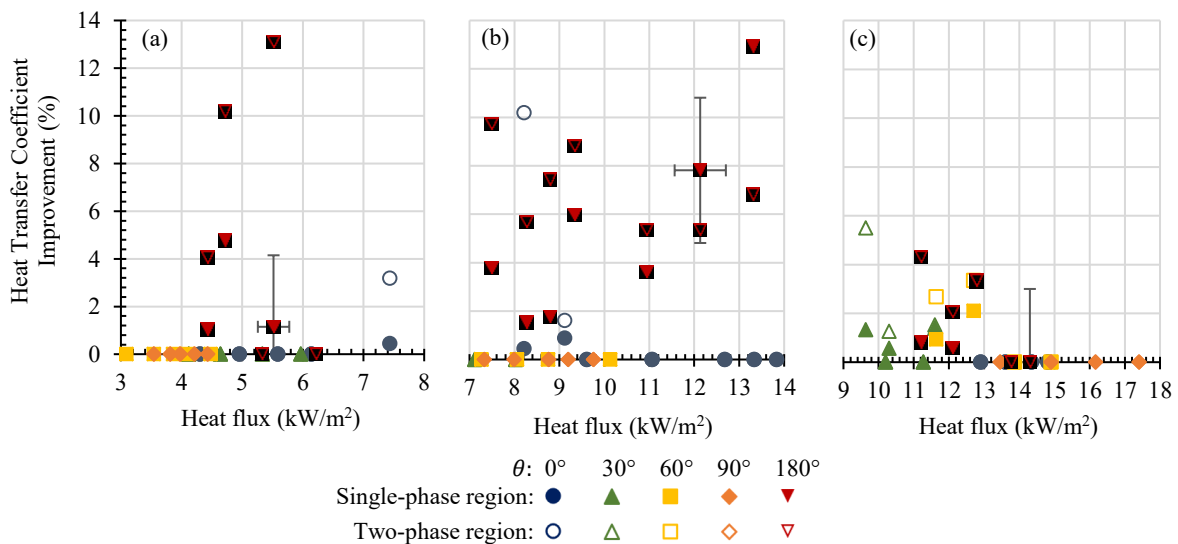

Figure 27: Average heat transfer coefficient improvement due major reverse flow events in the single-phase and two-phase region at a mass flux of (a) 10 kg/m²s, (b) 20 kg/m²s and (c) 40 kg/m²s

The heat transfer coefficient improvement in the two-phase region was typically greater than or equal to the improvement in the single-phase region at all rotations, mass fluxes and heat fluxes. The only two exceptions were at a rotation of $\theta = 180°$, mass flux of 20 kg/m²s and heat fluxes of 12.1 kW/m² and 13.3 kW/m² where the single-phase region had a greater heat transfer coefficient improvement than the two-phase region.

$\theta = 180°$ had the highest heat transfer coefficient improvement at all heat fluxes at a mass flux of 10 kg/m²s and 20 kg/m²s. The only exception was at a mass flux of 20 kg/m²s and heat flux of 8.2 kW/m² where $\theta = 0°$ had a heat transfer coefficient improvement of 10% in the two-phase region. The main reason for these observations was the lack of major reverse flow at $\theta = 30°$, 60° and 90°. $\theta = 0°$ had several major reverse flow events recorded at a mass flux of 10 kg/m²s and 20 kg/m²s but without the similar level of improvement in the heat transfer coefficient. It is expected that $\theta = 0°$ had high heat transfer coefficients due to the bubble separation from the

heated wall by a thick liquid layer. This separation resulted in a minimal improvement in the heat transfer coefficient when instability occurred. $\theta = 30°, 60°$ and $180°$ had non-zero heat transfer coefficients at a mass flux of 40 kg/m²s. $\theta = 30°$ and $60°$ had no major reverse flow events at a mass flux of 10 kg/m²s and 20 kg/m²s, this suggests that an increase in mass flux increased the likely hood of major reverse flow occurring but gives no indication of how mass flux effects the magnitude of the heat transfer coefficient improvement. Heat flux effects were only observed at a rotation of $\theta = 180°$ at a mass flux of 40 kg/m²s. An increase in heat flux resulted in an increase in the heat transfer coefficient improvement in most cases. It is expected that this might be due to the increased outlet vapour quality and larger portion of the heated wall in contact with the vapour slug. This region experiencing near dryout conditions grew as heat flux increased allowing for a larger improvement to occur. No heat flux effect was clearly defined at other mass fluxes or rotations.

6. CONCLUSION

In this study the influence of flow stability on the flow boiling heat transfer coefficient was considered for a rectangular micro/mini channel with a hydraulic diameter of 909 μm and an aspect ratio of 10. One-sided heating at different azimuth rotational angles (θ) in terms of gravity was investigated for a horizontal channel with FC-72 at a saturation temperature of approximately 56 °C. High-speed video footage was used to categorise different types of flow instability. Three instability types were identified: phase-mixing, minor reverse flow and major reverse flow, which were successfully matched with pressure transducer signal behaviour at the inlet and the outlet of the channel. The frequency of each instability type and its influence on the heat transfer coefficients in the single-phase (liquid) and two-phase regions were determined at mass fluxes of 10 kg/m²s, 20 kg/m²s and 40 kg/m²s, and at several heat flux conditions. Firstly, it was found that flow instability occurrences always improved the heat transfer coefficient, in both the liquid and two-phase regions of the channel. Secondly, it was observed that the prevalence of the different instability types was dependent on the channel azimuth rotation, mass flux and heat flux.

Azimuth rotations of $\theta = 0°$ and $180°$ (horizontal heated surfaces) had at least one instance of major or minor reverse flow at all heat flux and mass flux combinations. Rotated channels had no reverse flow or mild reverse flow at all heat fluxes at mass fluxes of 10 kg/m²s and 20 kg/m²s. Rotated channels experienced only major and minor reverse flow at a mass flux of 40 kg/m²s. The highspeed observations did not indicate a clear heat flux dependence. Rotated channels had a mass flux dependence with an increase in mass flux of 40 kg/m²s resulting in major and minor reverse flow.

$\theta = 180°$ had the highest instability frequency at all mass fluxes at both the inlet and outlet. An increase in heat flux typically resulted in a decrease in the instability frequency. The period of the instability events at $\theta = 180°$ were long compared to the other rotations suggesting that instability events occurred often and were intense enough to result in considerable surface cooling. The instability frequency at $\theta = 0°, 30°, 60°$ and $90°$ approached zero at most heat fluxes at mass fluxes of 10 kg/m²s and 20 kg/m²s. Reverse flow was observed at $\theta = 30°$ and $60°$ at the outlet at a mass flux of 40 kg/m²s.

Orientation had a substantial effect on the prevalence of flow instability, with horizontal channels experiencing all instability event types at almost all mass flux and heat flux combinations. Intermediate rotations, however, were largely stable at mass fluxes of 10 kg/m²s and 20 kg/m²s, while all instability types were observed at a mass

flux of 40 kg/m²s. Horizontal channels had similar instability frequencies at the various mass fluxes tested while intermediate channels had larger instability frequencies at 40 kg/m²s than at 10 kg/m²s and 20 kg/m²s, due to no instability observed at lower mass fluxes. Increases in heat flux typically decreased instability frequency for all rotations. Heat transfer coefficient improvements for horizontal channels were larger than for intermediate rotations at mass fluxes of 10 kg/m²s and 20 kg/m²s and similar at a mass flux of 40 kg/m²s. Heat transfer coefficient improvements were typically larger at lower mass fluxes when orientated horizontally, while intermediate rotations had no improvement at lower mass fluxes, again because no instability occurred. Heat transfer coefficient improvement were largely independent of heat flux for all rotations.

Two-phase mixing had the largest average improvement of up to 52% in the two-phase region. All instability event types had the greatest heat transfer coefficient improvement in the two-phase region at most rotations, mass fluxes and heat fluxes. Minor and major reverse flow typically had similar heat transfer coefficient improvement at all mass fluxes and heat fluxes. $\theta = 180°$ had the greatest heat transfer coefficient improvements, primarily due the low starting heat transfer coefficient because of the vapour slug in contact with the heated wall. A horizontal microchannel heated from above benefits the most from flow instability enhanced cooling.

Acknowledgements

References

[1] 3M, 3M Fluorinert Electronic Liquid FC-72 TDS_FINAL.pdf, (2019).

[2] K. Strąk, M. Piasecka, B. Maciejewska, Spatial orientation as a factor in flow boiling heat transfer of cooling liquids in enhanced surface minichannels, International Journal of Heat and Mass Transfer, 117 (2018) 375-387.

[3] Y. Lv, G. Xia, L. Cheng, D. Ma, Experimental investigation into unstable two phase flow phenomena during flow boiling in multi-microchannels, International Journal of Thermal Sciences, 166 (2021) 106985.

[4] L. Zhang, E.N. Wang, K.E. Goodson, T.W. Kenny, Phase change phenomena in silicon microchannels, International journal of heat and mass transfer, 48(8) (2005) 1572-1582.

[5] D. Paul, S. Singh, S. Mishra, Stability analysis of parallel channels in flow boiling system: Flow maldistribution and density wave oscillations, Chemical Engineering Science, 212 (2020) 115316.

[6] S. Wang, H.-H. Chen, C.-L. Chen, Enhanced flow boiling in silicon nanowire-coated manifold microchannels, Applied Thermal Engineering, 148 (2019) 1043-1057.

[7] W. Qu, I. Mudawar, Measurement and correlation of critical heat flux in two-phase micro-channel heat sinks, International Journal of Heat and Mass Transfer, 47(10) (2004) 2045-2059.

[8] R. Muwanga, I. Hassan, R. MacDonald, Characteristics of flow boiling oscillations in silicon microchannel heat sinks, Journal of Heat Transfer, 129(10) (2007) 1341-1351.

[9] S. Hong, C. Dang, E. Hihara, Experimental investigation on flow boiling in radial expanding minichannel heat sinks applied for low flow inertia condition, International Journal of Heat and Mass Transfer, 143 (2019) 118588.

[10] T.A. Kingston, J.A. Weibel, S.V. Garimella, An experimental method for controlled generation and characterization of microchannel slug flow boiling, International Journal of Heat and Mass Transfer, 106 (2017) 619-628.

[11] X. Li, T. Hibiki, Frictional pressure drop correlation for two-phase flows in mini and micro multi-channels, Applied Thermal Engineering, 116 (2017) 316-328.

[12] D. Brutin, F. Topin, L. Tadrist, Experimental study of unsteady convective boiling in heated minichannels, International journal of heat and mass transfer, 46(16) (2003) 2957-2965.

[13] L.X. Zong, G.D. Xia, Y.T. Jia, L. Liu, D.D. Ma, J. Wang, Flow boiling instability characteristics in microchannels with porous-wall, International Journal of Heat and Mass Transfer, 146 (2020) 118863.

[14] G.P. Celata, M. Cumo, D. Dossevi, R.T.M. Jilisen, S.K. Saha, G. Zummo, Visualisation of flow boiling heat transfer in a microtube, Heat and Mass Transfer, 47(8) (2011) 941.

[15] Z. Jiang, Z. Ma, R. Yan, L. Zhang, W. Sun, S. Bu, L. Pan, Experimental study on the flow boiling oscillation characteristics in a rectangular multiple micro-channel, Experimental Thermal and Fluid Science, 109 (2019) 109902.

[16] S. Lee, V.S. Devahdhanush, I. Mudawar, Investigation of subcooled and saturated boiling heat transfer mechanisms, instabilities, and transient flow regime maps for large length-to-diameter ratio micro-channel heat sinks, International Journal of Heat and Mass Transfer, 123 (2018) 172-191.

[17] Y. Kuang, W. Wang, J. Miao, H. Zhang, X.g. Yu, Non-linear analysis of nitrogen pressure drop instability in micro/mini-channels, International Journal of Heat and Mass Transfer, 147 (2020) 118953.

[18] J.A. Boure, A.E. Bergles, L.S. Tong, Review of two-phase flow instability, Nuclear Engineering and Design, 25(2) (1973) 165-192.

[19] J.S. Maulbetsch, P. Griffith, System-induced instabilities in forced convection flows with subcooled boiling, in: International Heat Transfer Conference Digital Library, Begel House Inc., 1966.

[20] T. Zhang, T. Tong, J.-Y. Chang, Y. Peles, R. Prasher, M.K. Jensen, J.T. Wen, P. Phelan, Ledinegg instability in microchannels, International Journal of Heat and Mass Transfer, 52(25-26) (2009) 5661-5674.

[21] P.K. Das, A.K. Das, 7 - Instability in Flow Boiling through Microchannels, in: S.K. Saha (Ed.) Microchannel Phase Change Transport Phenomena, Butterworth-Heinemann, 2016, pp. 257-286.

[22] Y. Ding, S. Kakaç, X.J. Chen, Dynamic instabilities of boiling two-phase flow in a single horizontal channel, Experimental Thermal and Fluid Science, 11(4) (1995) 327-342.

[23] H. Yüncü, O.T. Yildirim, S. Kakaç, Two-phase flow instabilities in a horizontal single boiling channel, Applied Scientific Research, 48(1) (1991) 83-104.

[24] L. Cheng, G. Xia, Fundamental issues, mechanisms and models of flow boiling heat transfer in microscale channels, International Journal of Heat and Mass Transfer, 108 (2017) 97-127.

[25] P. Balasubramanian, S.G. Kandlikar, Experimental study of flow patterns, pressure drop, and flow instabilities in parallel rectangular minichannels, Heat Transfer Engineering, 26(3) (2005) 20-27.

[26] M. Ozawa, H. Umekawa, K. Mishima, T. Hibiki, Y. Saito, CHF in oscillatory flow boiling channels, Chemical Engineering Research and Design, 79(4) (2001) 389-401.

[27] B. Maciejewska, M. Piasecka, A. Piasecki, The heat transfer and instabilities results during the onset of flow boiling in minichannels, E3S Web Conf., 128 (2019) 01016.

[28] T. Chen, S.V. Garimella, Local heat transfer distribution and effect of instabilities during flow boiling in a silicon microchannel heat sink, International Journal of Heat and Mass Transfer, 54(15) (2011) 3179-3190.

[29] X. Mingchen, J. Li, D. Chao, P. Qi, The effect of heating direction on flow boiling heat transfer of R134a in Micro-channels, Thermal Science, 26(2) (2017) 166-147.

[30] W. Li, Z. Chen, J. Li, K. Sheng, J. Zhu, Subcooled flow boiling on hydrophilic and super-hydrophilic surfaces in microchannel under different orientations, International Journal of Heat and Mass Transfer, 129 (2019) 635-649.

[31] S. Korniliou, C. Mackenzie-Dover, S. Harmand, G. Duursma, J.R.E. Christy, J.G. Terry, A.J. Walton, K. Sefiane, Local wall temperature mapping during flow boiling in a transparent microchannel, International Journal of Thermal Sciences, 135 (2019) 344-361.

[32] O. Engineering, Pressure Transducers, (2018).

[33] R.P. Madding, Emissivity measurement and temperature correction accuracy considerations, in: AeroSense '99, SPIE, 1999, pp. 9.

[34] P. Vasileiadou, K. Sefiane, T.G. Karayiannis, J.R.E. Christy, Flow boiling of ethanol/water binary mixture in a square mini-channel, Applied Thermal Engineering, 127 (2017) 1617-1626.

[35] Y. Wang, K. Sefiane, Effects of heat flux, vapour quality, channel hydraulic diameter on flow boiling heat transfer in variable aspect ratio micro-channels using transparent heating, International Journal of Heat and Mass Transfer, 55(9-10) (2012) 2235-2243.

[36] J. Barber, D. Brutin, K. Sefiane, J.L. Gardarein, L. Tadrist, Unsteady-state fluctuations analysis during bubble growth in a "rectangular" microchannel, International Journal of Heat and Mass Transfer, 54(23-24) (2011) 4784-4795.

[37] Y. Li, H. Wu, Y. Yao, Enhanced flow boiling heat transfer and suppressed boiling instability in counter-flow stepped microchannels, International Journal of Heat and Mass Transfer, 194 (2022) 123025.

[38] K. Luo, W. Li, J. Ma, W. Chang, G. Huang, C. Li, Silicon microchannels flow boiling enhanced via microporous decorated sidewalls, International Journal of Heat and Mass Transfer, 191 (2022) 122817.

[39] W. Li, K. Luo, C. Li, Y. Joshi, A remarkable CHF of 345W/cm2 is achieved in a wicked-microchannel using HFE-7100, International Journal of Heat and Mass Transfer, 187 (2022) 122527.

[40] G. Criscuolo, W.B. Markussen, K.E. Meyer, M.R. Kærn, High heat flux flow boiling of R1234yf, R1234ze(E) and R134a in high aspect ratio microchannels, International Journal of Heat and Mass Transfer, 186 (2022) 122215.

[41] Y.A. Çengel, A.J. Ghajar, Heat and mass transfer : fundamentals & applications, Fifth edition. ed., McGraw Hill Education, New York, NY, 2015.

[42] R.J. Moffat, Describing the uncertainties in experimental results, Experimental Thermal and Fluid Science, 1(1) (1988) 3-17.

[43] Y. Wang, K. Sefiane, S. Harmand, Flow boiling in high-aspect ratio mini- and micro-channels with FC-72 and ethanol: Experimental results and heat transfer correlation assessments, Experimental Thermal and Fluid Science, 36 (2012) 93-106.

[44] S.G. Kandlikar, Nucleation characteristics and stability considerations during flow boiling in microchannels, Experimental Thermal and Fluid Science, 30(5) (2006) 441-447.

[45] G. Xia, Y. Lv, L. Cheng, D. Ma, Y. Jia, Experimental study and dynamic simulation of the continuous two-phase instable boiling in multiple parallel microchannels, International Journal of Heat and Mass Transfer, 138 (2019) 961-984.

[46] M. Vermaak, J. Potgieter, J. Dirker, M.A. Moghimi, P. Valluri, K. Sefiane, J.P. Meyer, Experimental and Numerical Investigation of Micro/Mini Channel Flow-Boiling Heat Transfer with Non-Uniform Circumferential Heat Fluxes at Different Rotational Orientations, International Journal of Heat and Mass Transfer, 158 (2020).